Accepted Manuscript

Detection of nitroaromatics based on aggregation induced emission of barbituric acid derivatives

Han-Jun Zhang, Yan Tian, Fu-rong Tao, William Yu, Kai-Yue You, Lin-Rui Zhou, Xi Su, Tian-duo Li, Yue-Zhi Cui

PII:	S1386-1425(19)30558-X
DOI:	https://doi.org/10.1016/j.saa.2019.117168
Article Number:	117168
Reference:	SAA 117168
To appear in:	*Spectrochimica Acta Part A: Molecular and Biomolecular Spectroscopy*
Received date:	14 December 2018
Revised date:	9 May 2019
Accepted date:	26 May 2019

Please cite this article as: H.-J. Zhang, Y. Tian, F.-r. Tao, et al., Detection of nitroaromatics based on aggregation induced emission of barbituric acid derivatives, Spectrochimica Acta Part A: Molecular and Biomolecular Spectroscopy, https://doi.org/10.1016/j.saa.2019.117168

Detection of Nitroaromatics Based on Aggregation Induced Emission of Barbituric Acid Derivatives

Han-Jun Zhang, Yan Tian, Fu-rong Tao, William Yu, Kai-Yue You, Lin-Rui Zhou, Xi Su, Tian-duo Li, Yue-Zhi Cui*

School of Chemical and Pharmaceutical Engineering, Qilu University of Technology, Jinan 250353, P. R. China.

Tel: +86 531 89631208; Fax: +86 531 89631760;

E-mail address: yuezhicui@163.com

Abstract

Barbituric acid derivatives with typical aggregation induced emission (AIE) are reported. Their emission wavelengths varied with water fraction of their solution. UV-visible absorption spectroscopy and theoretical calculations revealed the intramolecular charge transfer (ICT) possibility from donor to acceptor and the mechanism was confirmed as a restriction of intramolecular motion (RIM). The AIE properties were affected by the different substituents on barbituric acid. When the molecular volume increased, the AIE effect decreased. Fluorescent quenching mechanism was applied to detect nitroaromatic explosives. For 2,4,6-trinitrophenol (PA), one of the derivatives 5-(4-diphenylamino styrene)-1,3-diphenyl-barbituric acid in THF/H_2O mixture (1:9, v/v), showed amplified fluorescence quenching with a maximum Stern–Volmer quenching constant of 4.1×10^4 M^{-1}. The solid phase paper test based on 5-(4-diphenylamino styrene)-1,3-diphenyl-barbituric acid also showed a superior sensitivity toward PA both in vapor and solution.

Key words: Aggregation induced emission (AIE); Intramolecular charge transfer (ICT); Restriction of intramolecular motion (RIM); Fluorescent sensor;

1. Introduction

Tang's team firstly reported the aggregation-induced emission (AIE) phenomenon in 2001[1, 2], which is opposite to the aggregation-caused quenching (ACQ) [3, 4]. The main source of AIE effect is the inhibition of the appearance of π-π stacking between molecules [5].A common feature of these materials is that they do not emit in molecular solution but emit strong fluorescence in the aggregated state. Therefore AIE provides a new avenue for applications in optoelectronic devices, bio/chemical sensors, and bioimaging [6-8].

However, typical compounds with AIE require cumbersome multi-step synthesis, and often result in bulky and structurally complex AIE materials. Therefore, exploring luminescent materials with AIE-active but simple structures is still interesting and valuable.

Herein, we recommend three AIE active and structurally simple luminescent materials based on barbituric derivatives. The powerful aggregation ability of barbituric acid units through intermolecular hydrogen bonding interactions (N-H···O) has been well documented in the literature [9, 10]. Therefore, we focused on the relationship between AIE effect and molecular structure of three barbituric acid derivatives.

Nitroaromatic explosives are widely used in many fields because they are easy to prepare and transport, and they are powerful. The detonation of explosives usually causes damages to the environments, which in turn affects people's health. Studies disclose that the explosive residues can pollute the air, soil and water systems. Long-term exposure to these residues can cause various diseases such as skin diseases, respiratory system problems, abnormal liver function and cancer [11-15]. All of these have aroused the concern about how to effectively detect them.

Triphenylamine naturally as a three-dimensional freely rotatable structure, and the internal energy consumption is large that makes the fluorescence quantum yield low, but the structure of triphenylamine is easily to be modified, and the fluorescence quantum yield is generally high after modification. Triphenylamine also exhibits distinct donor characteristics, which should facilitate interaction with electron-deficient nitroaromatic compounds. However, there are few reports on triphenylamines for photoluminescence (PL)-based explosives detection.

Most fluorescent sensors for detecting nitroaromatics cannot be operated in aqueous media, but compounds with AIE can solve this problem nicely. In this project, we designed

and synthesized barbituric derivative fluorescence sensors, which can generate aggregates in high water content and can thus be used for the detection of nitroaromatics in aqueous media.

2. Experimental section

2.1 Materials

Triphenylamine (Aladdin, 99%), dimethylformamide (DMF) (Aladdin, 99%), barbituric acid (Aladdin, 98%), diphenylurea (Jiuding Chemical, 99%), malonyl chloride (Aladdin, 99%), 1, 3-dimethyl-barbituric acid (Aladdin, 99%) were used without further purification. DMF is usually dried sequentially by molecular sieves (4 Å), sodium sand and CaH_2 successively, and distilled prior to use.

2.2. Characterizations

Absorption spectra were recorded by a UV-2500 spectrometer. The fluorescence spectra were measured with an F-4600 fluorescence spectrophotometer. The fluorescence quantum yield of the solid is commissioned by the compass test platform. The ^{1}H and ^{13}C NMR spectra were recorded on AVANCE II 400 spectrometer using deuterated dimethyl sulfoxide (DMSO-d_6). FT-IR spectra were obtained recorded by a Nicolet 380 spectrometer using the KBr pellet method. The scanning electron microscope images were obtained with Quanta 200 environmental scanning electron microscope (SEM, FEI Company).

2.3 Calculation

The geometric and electronic structures of the three compounds were calculated at the B3LYP level with Density Functional Theory (DFT).

2.4 Synthesis of compounds

The target luminescent materials were synthesized by (1,3-dimethyl, 1,3-diphenyl) barbituric acid and N, N-diphenylamine benzaldehyde condensation reaction (scheme 1).

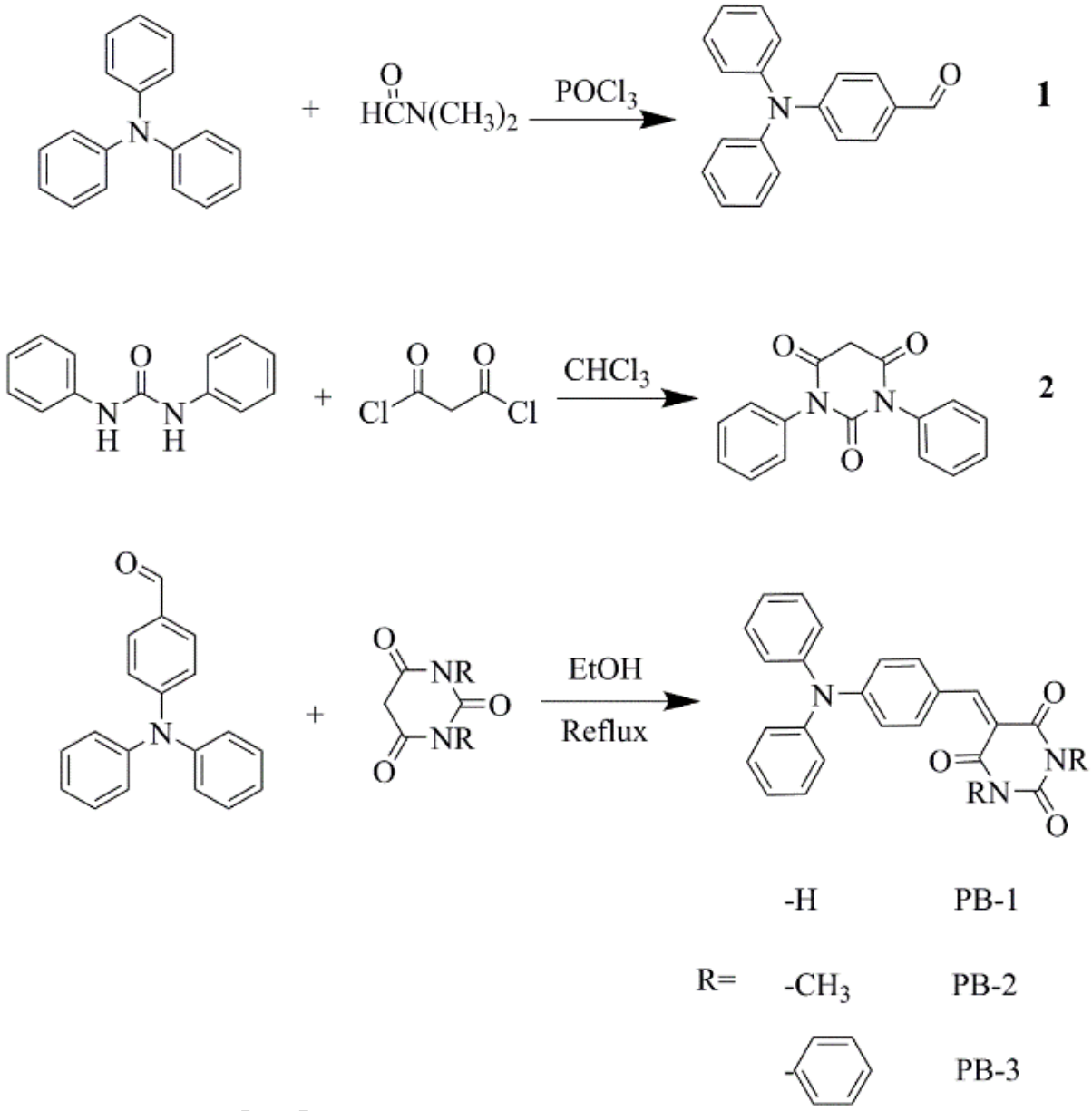

Scheme 1. Synthetic routes to PB-1, -2, and -3

2.4.1. Synthesis of 4-(diphenylamino)-benzaldehyde (1)

2 ml of dry DMF (25.7 mmol) was added into 5 ml of phosphorus oxychloride ($POCl_3$) (54 mmol), at 0^{o}C, and remained for 15 min, then triphenylamine (1 g, 4 mmol) was added with stirring. The mixture was heated to 45^{o}C for 2.5 h. After being cooled down, the clear red solution was dropped into ice water. The resulting mixture was filtered, washed and redissolved in dichloromethane. This solution was washed with water (150 ml) and dried with magnesium sulfate, after solvent evaporation, the oily liquid recrystallized into

acetaldehyde in ethyl acetate. Yield: 0.78g (80%). ^{1}H NMR (400 MHz, DMSO-d_6): δ 9.82 (s, 1H), 7.74 - 7.61 (m, 2H), 7.35 (t, *J* = 7.7 Hz, 4H), 7.22 - 7.13 (m, 6H), 7.07 - 6.96 (m, 2H) (Fig. S1).

2.4.2. Synthesis of 1, 3-diphenyl barbituronic acid (2)

Malonyl chloride (33.3 mg, 2 mmol) was added to N, N-diphenyl urea (424.5 mg, 2 mmol) with 6 ml $CHCl_3$, and the mixture was heated to 80^{o}C for 4 h. Then the reaction mixture was extracted with dichloromethane and dried over Na_2SO_4. After filtration, the filtrate was concentrated under reduced pressure and further purified by column chromatography. Yield: 343.1 mg (75%). ^{1}H NMR (400 MHz, DMSO-d_6): δ 7.45 (d, *J* = 7.5 Hz, 3H), 7.41 (d, *J* = 7.5 Hz, 1H), 7.28 (d, *J* = 7.4 Hz, 3H), 4.01 (s, 1H) (Fig. S2).

2.4.3. Synthesis of 5-(4-diphenylamino styrene)-barbituric acid (PB-1), 5-(4-diphenylamino styrene)-1,3-dimethyl-barbituric acid (PB-2), 5-(4-diphenylamino styrene)-1,3-diphenyl -barbituric acid (PB-3)

The synthetic steps of PB-1 and PB-2 have been published in the previous papers of our group [4], so the synthesis and characterization of PB-3 are discussed here.

PB-1: ^{1}H NMR (400 MHz, DMSO-d_6) δ (ppm): 8.42 (s, 1H), 8.31 (d, *J* = 8.9 Hz, 2H), 7.97 (s, 1H), 7.80 (s, 1H), 7.40 (t, *J* = 7.7 Hz, 4H), 7.24 (t, *J* = 6.3 Hz, 6H), 6.94 (d, *J* = 8.9 Hz, 2H) (Fig. S3). ^{13}C NMR (126 MHz, DMSO-d_6) δ 155.13, 152.67, 151.2, 150.69, 145.51, 138.13, 130.58, 127.21, 126.48, 124.37, 117.30, 113.99 (Fig. S4). FT-IR (KBr, cm^{-1}): 1672 (C=O) (Fig. S5). (The FT-IR of the C=O bond present in the molecule of the barbituric acid derivative is around 1670 cm^{-1}). HRMS (ESI) *m*/*z*: $[M + H]^+$ calcd for $C_{23}H_{17}N_3O_3$, 383.41; found, 384.1278(Fig. S6).

PB-2: ^{1}H NMR (400 MHz, DMSO-d_6) δ (ppm): 8.44 (s, 1H), 8.24(d, 2H), 7.38 (t, 4H), 7.23 (m, 6H), 6.95 (d, 2H), 3.40 (d, 6H) (Fig. S7). ^{13}C NMR (126 MHz, DMSO-d_6) δ 161.37, 155.98, 152.71, 151.62, 145.49, 138.05, 130.59, 127.20, 126.50, 124.42, 117.30, 113.83, 28.77 (Fig. S8). FT-IR (KBr, cm^{-1}): 1667(C=O) (Fig. S9). (The FT-IR of the C=O bond present in the molecule of the barbituric acid derivative is around 1670 cm^{-1}). HRMS (ESI) *m*/*z*: $[M + H]^+$ calcd for $C_{25}H_{21}N_3O_3$, 411.462; found,412.1557 (Fig. S10).

PB-3: A mixture of 1 (0.447 g, 3 mmol) and 1, 3-diphenyl barbituronic acid (0.840 g, 3 mmol) in (10ml) ethanol was refluxed for 4 h. After filtration, the filtrate was concentrated under reduced pressure and further purified by column chromatography (ethyl acetate: petroleum ether = 2:1). Yield: 1.158 g (90%). ^{1}H NMR (400 MHz, DMSO-d_6) δ (ppm): 8.30

(s, 1H), 8.23 (d, *J* = 8.4 Hz, 2H), 7.49 - 7.38 (m, 12H), 7.34 (d, *J* = 7.5 Hz, 6H), 7.24 (d, *J* = 8.4 Hz, 8H), 6.74 (d, *J* = 8.5 Hz, 2H) (Fig. S11). ^{13}C NMR (126 MHz, DMSO-d_6) δ 163.54, 161.57, 156.45, 152.84, 145.37, 138.22, 130.58, 129.60, 129.47, 129.24, 128.72, 127.25, 126.59, 125.10, 117.15, 114.39 (Fig. S12). FT-IR (KBr, cm^{-1}): 1667 (C=O) (Fig. S13). (The FT-IR of the C=O bond present in the molecule of the barbituric acid derivative is around 1670 cm^{-1}). HRMS (ESI) *m*/*z*: $[M + H]^+$ calcd for $C_{35}H_{35}N_3O_3$,535.686; found,536.1873 (Fig. S14).

3 Results and discussion

3.1 Optical properties

Fig. 1 shows absorption spectra of PB-1, -2, and -3 at different THF/H_2O percentages (water fraction f_w = 0, 30, 50, 70%). The results show that the absorbance decreases with the increase of water fractions and the reason may be that the degree of torsion of the molecules increases with the increase of water fractions, leading to a weak intramolecular charge transfer. The absorption band in the range of 270 to 300 nm is assigned to the π-π* electronic transition of the corresponding benzene ring unit. The absorption peaks at 454, 455 and 464 nm (for PB-1, -2, and -3, respectively) can be attributed to the ICT from diphenylamine units to part of barbiturates [16].

At the same time, it was also founded that absorption spectra of the PB-1 had a wide and relatively weak peak at around 350 nm, which may be consistent with the characteristics of n-π* transition. This mechanism can be depicted in Fig. 2. As water is added, PB-1 undergoes tautomerization from the keto to the enol structure.

The IR spectra of the three compounds were measured to verify the tautomerization of PB-1, as shown in Fig.3. A wide peak at 3413~3418 cm^{-1} appeared in all the three spectra, which may be attributed to the trace of water in the samples. It is noteworthy that a unique peak around 3220 cm^{-1} appeared in PB-1, while it is absent in PB-2 and PB-3. Reasonably, the peak at 3220 cm^{-1} is attributed to the hydroxyl groups in the enol structure of PB-1. However, for PB-2 and PB-3, with the hydrogen atom in NH group is replaced by a methyl group and a phenyl group, respectively, cannot undergo tautomerization from the keto to the enol structure, thus there is no hydroxyl group to produce the IR peak at 3200 cm^{-1}.

In the enol structure of PB-1, the lone pairs of electrons on the N atom can generate n-π* transitions with N=C double bonds, thus produces the absorption peak at 350 nm.

Accordingly, without enol structure for PB-2 and -3, there is no n-π* transitions, thus the peak at 350 nm is absent in the absorption spectra of PB-2 and -3.

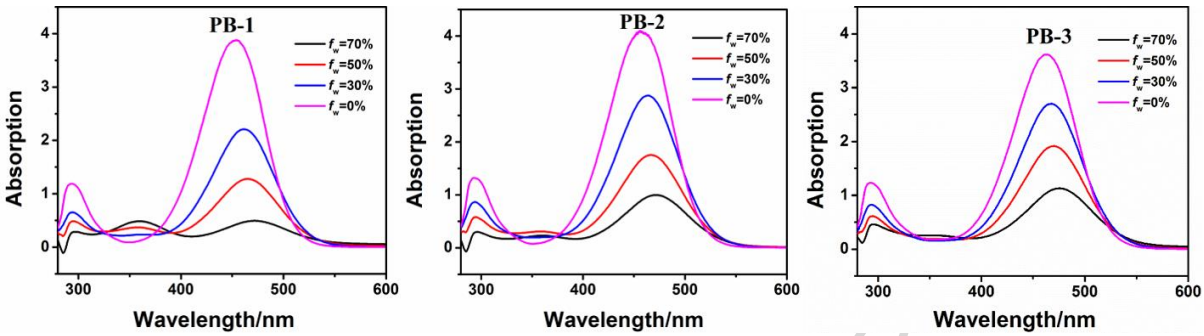

Fig. 1. UV-visible absorption spectra of PB-1, -2, and -3 in different THF/H_2O percentage solutions (solution concentration: 10^{-4}M).

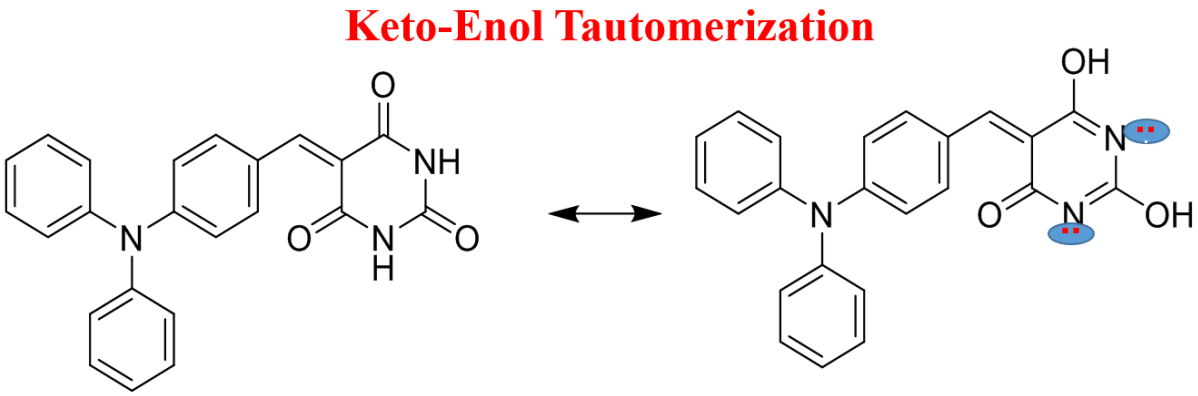

Fig. 2. Mechanism of PB-1 tautomerism.

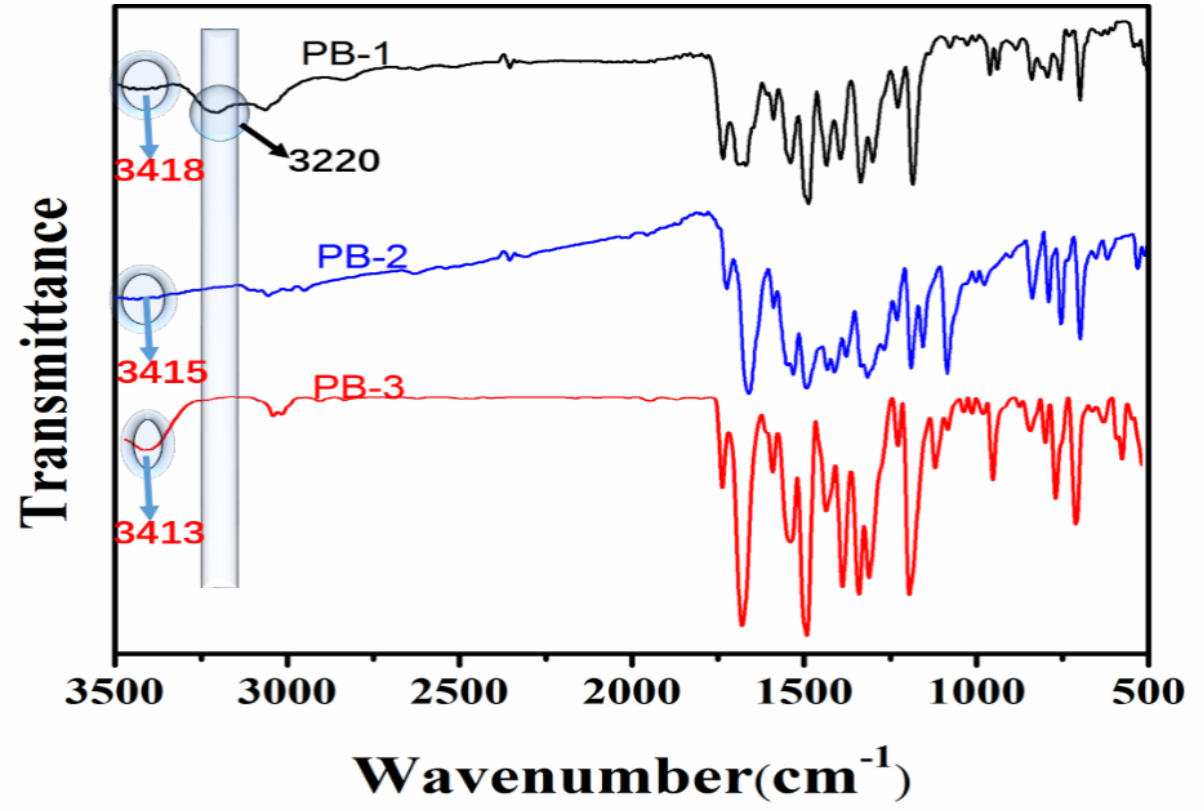

Fig. 3. FT-IR spectra of PB-1, PB-2 and PB-3.

3.2 AIE effect

It can be seen from the photograph that the emissivity of compounds PB-1, -2, and -3 is weak in the low concentration of pure THF (Fig. 4), because the intermolecular interaction in solution is relatively weak, so they rotate freely in solution state and energy is expended in a non-radiative transition showing a weak fluorescence[17].

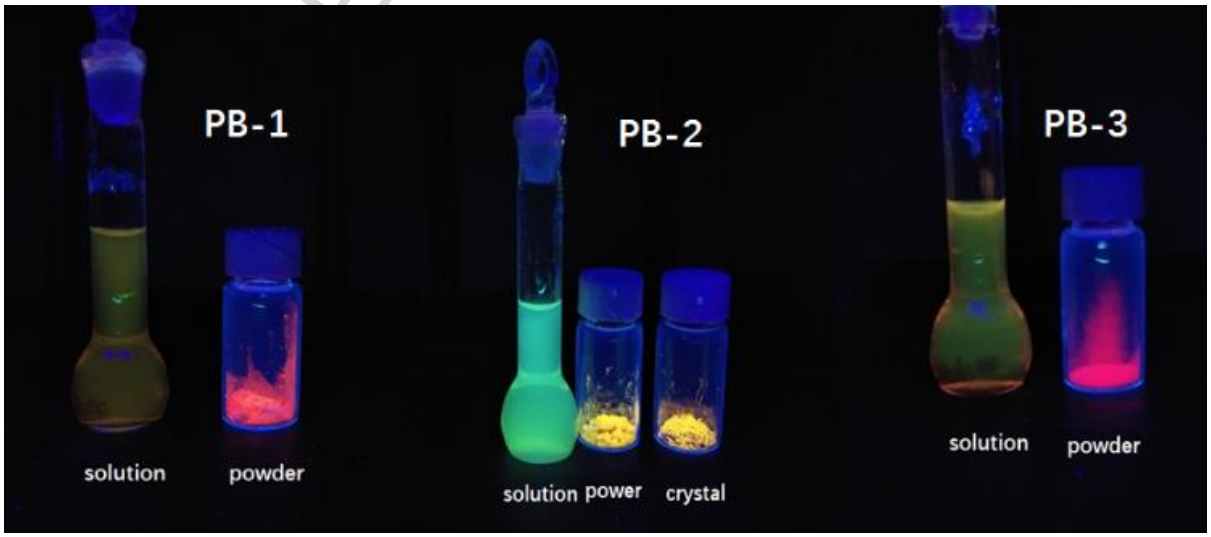

Fig.4. Fluorescence photographs of PB-1, -2, and -3 under ultraviolet light irradiation in different states (365 nm).

To test whether PB-1, -2, and -3 have AIE property, their PL behavior in THF/H_2O of different water fractions (f_w) was investigated with the concentration of PB series of $10^{-4}M^{-1}$ (Fig.5). PB-1, -2, and -3 exhibited weak emissions at 619.0, 628.0 and 634.0 nm in pure THF (Table 1).

Table 1 Optical properties of PB-1, -2, and -3.

	Solution / THF			**Aggregation solution (f_w = 90%)**		**Solid powder**	I_A/I_P
	λ_{abs} / nm	λ_{em} / nm	Stokes shift / nm	λ_{em} / nm	λ_{em} / nm	Φ_F / %	
PB-1	454.5	619.0	164.5	625.0	629.0	41.50%	7.2
PB-2	455.5	628.0	172.5	620.0	589.0	23.27%	3.6
PB-3	464.0	634.0	170	638.0	672.0	32.34%	2.1

Note: I_A is the fluorescence intensity in the aggregation solution, I_P is the fluorescence intensity in pure THF.

Significantly, PB-1 exhibits enhanced AIE effect compared to PB-2 and PB-3: in aggregation solution, the luminescence intensity of PB-1 is 7.2-fold higher than that in THF. In addition, the solid fluorescence quantum yields of PB-1, PB-2, and PB-3 were 41.50%, 23.27%, and 32.34%, respectively [18]. As mentioned previously, the better AIE performance of PB-1 is attributable to H-bonding, which helps to further solidify the molecular conformation of the aggregated state and block the non-radiative transition.

We found that the AIE effect is related to the molecular structure of barbituric derivatives, which as the volume of barbituric acid derivatives increased, the AIE index (I_A/I_P) decreased (Table 1). The aggregation induced fluorescence indexes of PB-1, PB-2 and PB-3 are 7.2, 3.6 and 2.1, respectively. Fluorescence intensity of PB-3 is weaker than those of PB-1 and PB-2 in aggregation state, but stronger than those of PB-1 and PB-2 in pure solution, fluorescence intensity of PB-2 is weaker than that of PB-1 in aggregation, but stronger than that of PB-1 in

pure solution. The reason is that large steric hindrance of the larger group make it difficult to rotate freely in pure solution. On the other hand, in the state of aggregation of groups with larger molecular spacing, the intermolecular interaction is weakened.

We also investigated the effect of the emission spectra of PB-1, -2 and -3 by varying the amount of glycerol in the THF-glycerol mixture. As seen from Fig. S15, the fluorescence intensity increases with increased glycerol contents in the THF-glycerol mixtures, because the intramolecular rotation is limited by more glycerol, which attenuates the non-radiative transition process and enhances the emission.

We carefully analyzed the AIE behavior of the three compounds. Compound of PB-1 exhibits a more complicated tendency with the increase of f_w. The emission peak of PB-1 red-shifts from 619.4 nm to 648.4 nm when f_w increases from 0% to 70%. Furtherly, it blue-shifts to 624.4 nm as f_w increase to 90%. It is known from section 3.1 that PB-1 produces the tautomerization from keto to enol structure, so the intermolecular hydrogen bond (N-H···O) interaction exists, which increases the solubility of PB-1 in aqueous medium. Therefore, when $f_w \leq 70\%$, the PB-1 molecule is completely dissolved in the mixed solution ($C_{PB-1}=10^{-4}M^{-1}$), and the increased f_w enhances the polarity of mixture, generating the red-shifted emission due to the ICT effect. When $70\% < f_w \leq 90\%$, the tightly aggregated particles formed, in which the free rotation of the molecules was restricted, resulting in the so-called RIR mechanism. By this mechanism, the emission intensity increased abruptly with an AIE effect of 7.2.

As show in Fig. 5, PB-2 and PB-3 have similar behaviors with the f_w changes. When $f_w \leq$ 40% for PB-2 and $f_w \leq 20\%$ for PB-3, the molecules are still completely soluble in the mixture solution. With hydrophobic methyl and phenyl groups on the N atom of barbituric acid, respectively, they exhibits lower solubility than PB-1. In the resolvable range, the increase in f_w enhances the polarity of the mixture, the fluorescence intensity decreases due to ICT [19], while the emission wavelength is accompanied by a red shift. However, as the water content increases ($40\% < f_w \leqslant 80\%$ for PB-2 and $20\% < f_w \leq 60\%$ for PB-3), the molecules pack into loose aggregates firstly, and the polarity of the micro-environment of the luminescent molecule is reduced due to self-wrapping, thereby generates blue-shift of the emission wavelength. Meanwhile, the loose packing does not restrict the free rotation of the molecules, which leads to the continuing decrease in fluorescence intensity with f_w increases.

When 80%＜f_w≤90% for PB-2 and 60%＜f_w≤90% for PB-3, the molecules begin to pack tightly into nano-aggregates due to the strong intermolecular forces, and the RIR mechanism takes effect. As a result, the emission wavelength red-shifts while the fluorescence intensity increases.

To verify that the gradual decrease in fluorescence at low f_w values is due to ICT, emission spectra were recorded in different solvents of different polarities. As can be seen from Fig. S16, The fluorescence intensity of the barbituric acid derivatives PB-1, PB-2 and PB-3 decreased with the increase of the polarity of different solutions and the emission wavelength was red-shifted. It was verified that the fluorescence decreased gradually at low f_w values due to ICT.

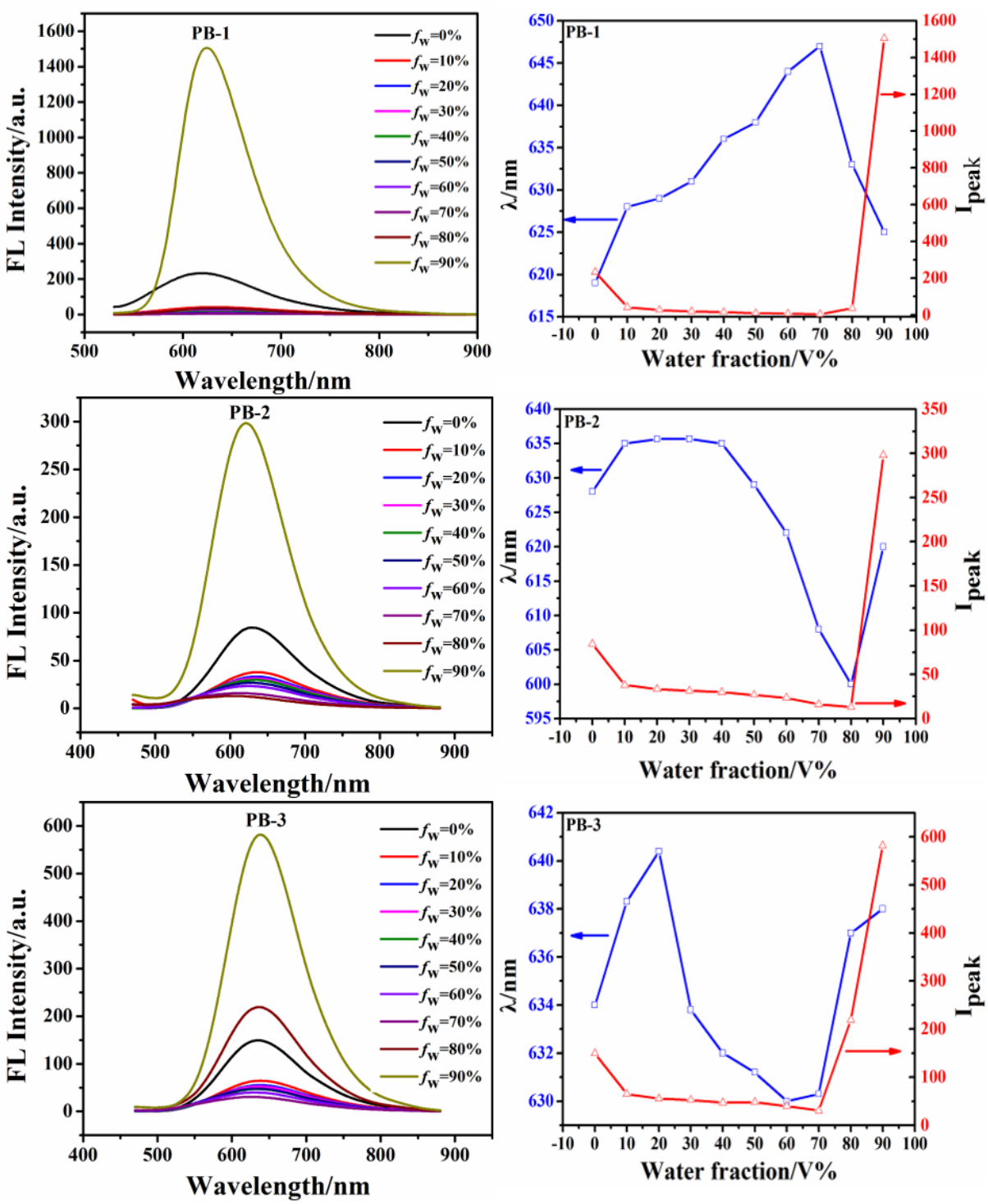

Fig. 5. Left: Fluorescence spectra of PB-1, -2 and -3 in different water content (f_w) of THF/H_2O mixture; Right: emission peak (square) and emission intensity (triangle) relative to the water fraction in the mixture. The excitation wavelengths were 450, 450 and 430 nm, respectively.

The fluorescence photos of PB-1, -2 and -3 under UV irradiation (365 nm) in different water contents are shown in Fig. 6. The fluorescence intensity of the solution first decreases,

then increases significantly, and the color of luminescence changes significantly, from yellow-green emission to orange or red emission.

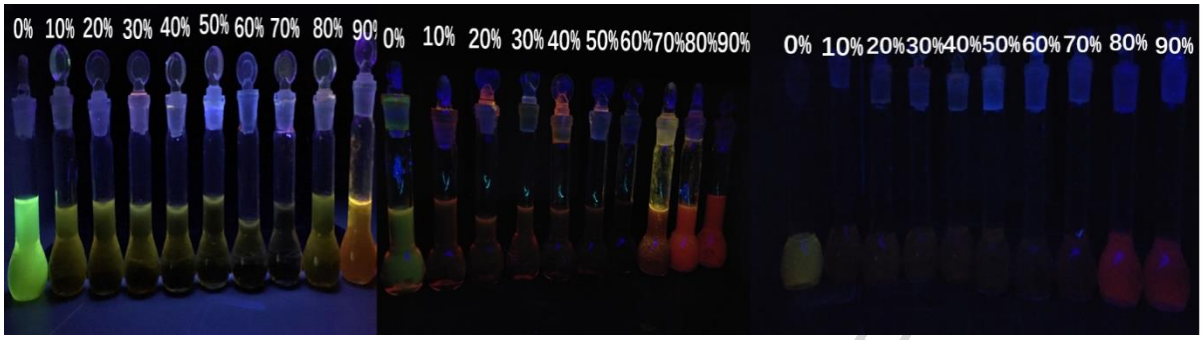

Fig. 6. Fluorescent photographs of PB-1, -2 and -3 in different f_w THF/H_2O mixed solvents irradiated by a 365 nm ultraviolet lamp (solution concentration: 10^{-4}M)

Scanning electron microscopy (SEM) and dynamic light scattering (DLS) were used to detect the morphology and size of nano-aggregates in different f_w solvents (Fig. 7) which show the presence of spherical and blocky aggregates. As shown in Fig. 7, the solution was uniformly stable at a water content of 90%, and the average diameters (d) of the PB-1, -2 and -3 aggregates were 645.2, 346.0 and 426.0 nm, respectively. These data indicate that the enhanced emission of the compounds is related to the formation of nano-aggregates.

The intermolecular hydrogen bond (N-H···O) interaction exists in the barbituric acid unit on PB-1 due to the tautomerization from the keto to the enol structure, resulting in the larger size of aggregates. On the contrary, without intermolecular hydrogen bond, both the aggregate sizes of PB-2 and -3 are much smaller than that of PB-1.

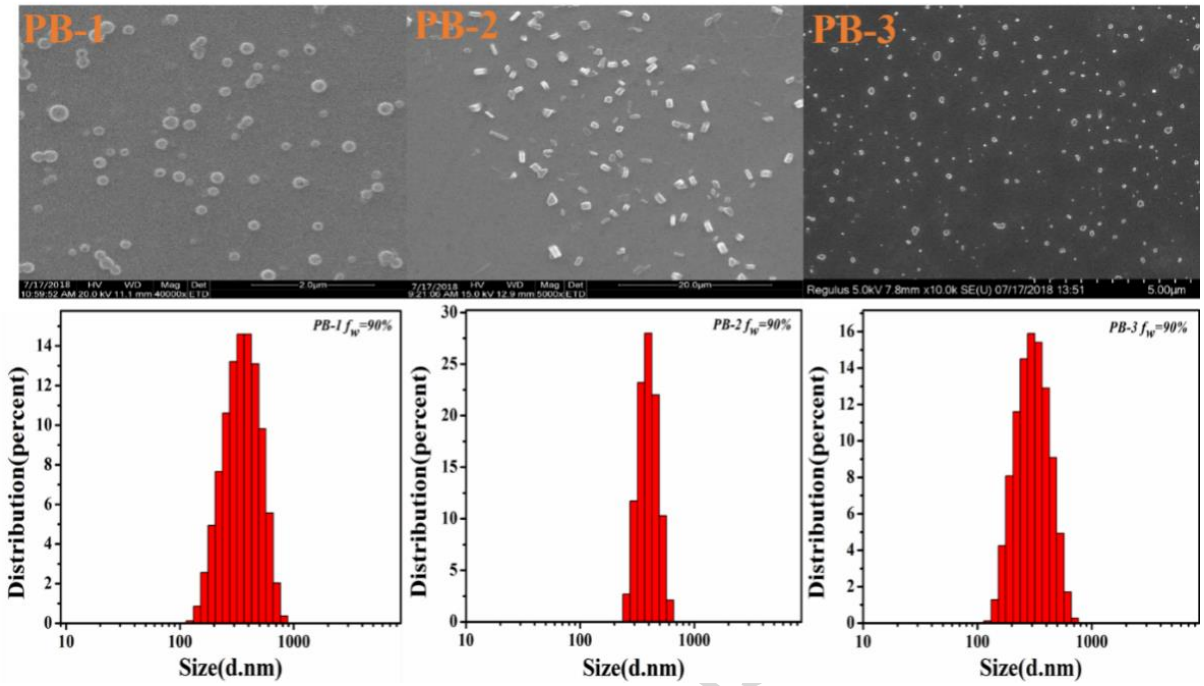

Fig. 7. SEM images and particle size distribution histograms of PB-1, -2, -3 in a THF/H_2O mixture (f_w = 90%) (solution concentration: 10^{-4}M).

3.2 Theoretical calculation

In order to better understand their optical properties, we calculated the frontier molecular orbitals using the DFT of the B3LYP/6-31G (d) basis set [22, 23]. Optimized geometry and HOMO, LUMO energy levels of PB-1, PB-2 and PB-3 are given in Fig. 8 and Fig. 9. They exhibit highly distorted conformations that facilitate active intramolecular rotation of the phenyl group in solution, thereby effectively dissipating exciton energy for weak emission in the solvent. Its HOMO is located on the electron-donor triphenylamine, and LUMO is mainly distributed on the electron-acceptor barbituric acid. The above results further illustrate the occurrence of an ICT process from the donor to the acceptor moiety, which is consistent with the observed optical properties [24].

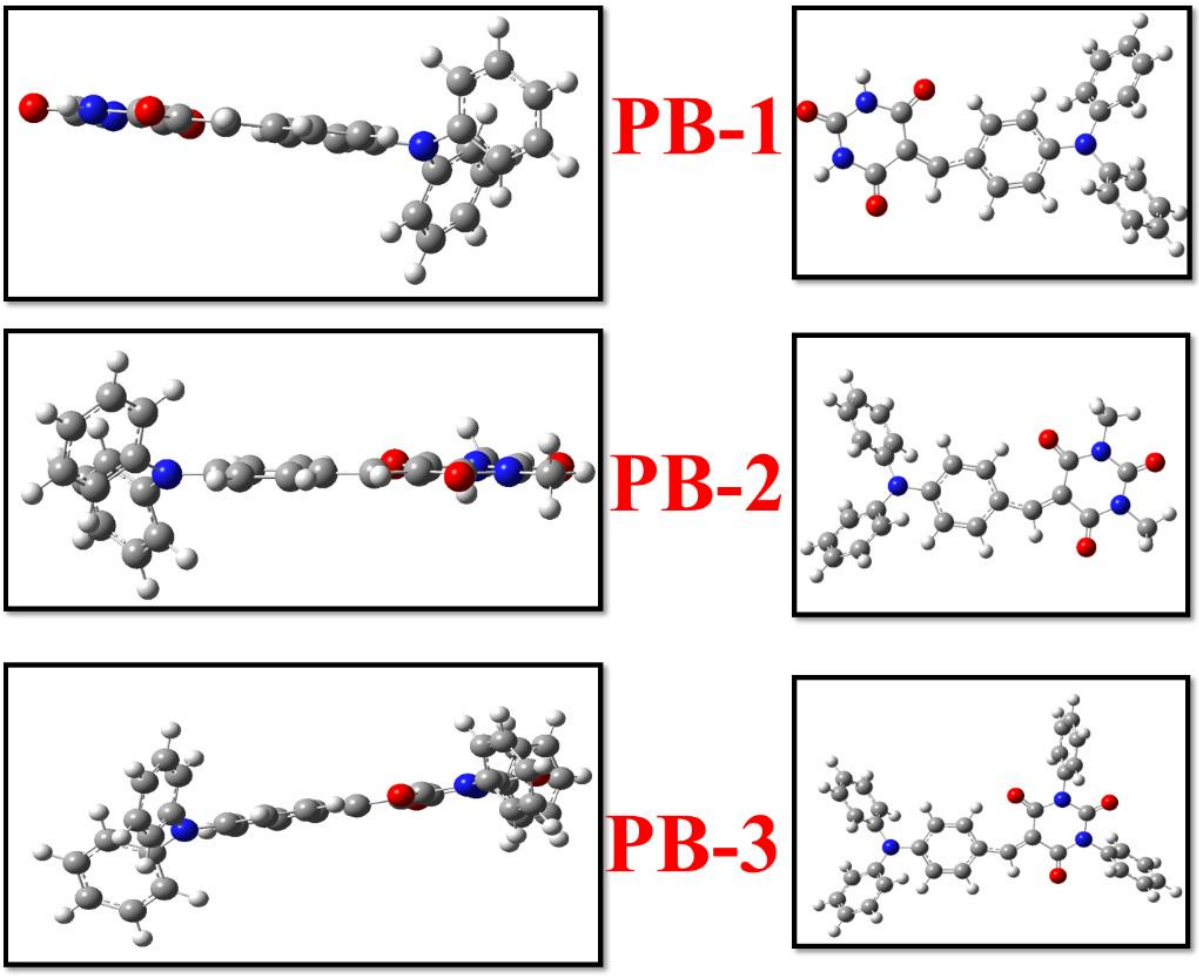

Fig. 8. Optimized molecular ground state geometries of PB-1, -2, and -3.

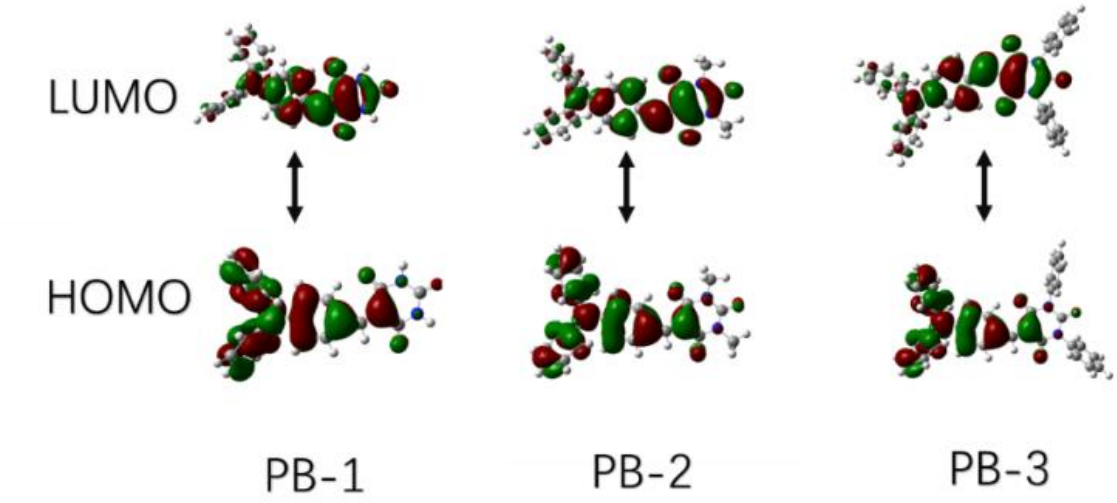

Fig. 9. Electron density distributions of LUMO and HOMO molecular orbitals of PB-1, -2, and -3.

3.3 Compound fluorescence enhancement mechanism

Single crystal X-ray diffraction (SXRD) analysis can provide direct evidence of the molecular conformation and packing structure of the compound. The single crystal of PB-2 was successfully cultured before, but it was unsuccessful for PB-1 and PB-3 crystals. Since our group already has the single crystal data of PB-2, we cite them directly here. The specific analysis of Fig. 10 has been presented in the previous work [4] of our group.

According to our previous work, the reason why PB-1, -2, and -3 weakly emit when the particles dissolved in a solvent is due to the free rotations and vibrations inside molecules. Intramolecular interaction inhibits the process of radiation decay and promotes enhanced emission, which is primarily due to the limited intramolecular motion and some specific molecular packing models, such as herringbone stacking [25, 26].

In the dilute solution, the steric hindrance in the molecule reduces the π-conjugation, PB-1, -2, and -3 are almost isolated and adopted a twisted conformation. Movements such as rotation, vibration, and stretching within the molecule consume the energy of the excited state and suppress the decay process of the radiation. While in the aggregate state, intramolecular vibration or rotation is locked by the interaction forces between molecules, such as C-H···O, C=O···C and C=O···N and many CH··π interactions. Therefore, intramolecular motion is significantly suppressed, hindering the non-radiative process.

In general, it can be said that the mechanism for enhancing PB-1, PB-3 emission is the restriction of intramolecular motion (RIM) caused by molecular aggregation. Additionally, PB-2 also shows a herringbone stacked conformation in the crystal, Herringbone stacking and RIM are considered the reasons for the enhancement of PB-2 emission. Therefore, according to the results of SEM and DLS, the formation of nano-aggregates of PB-1, -2 and -3 at high f_w can be attributed to the phenomenon of fluorescence enhancement.

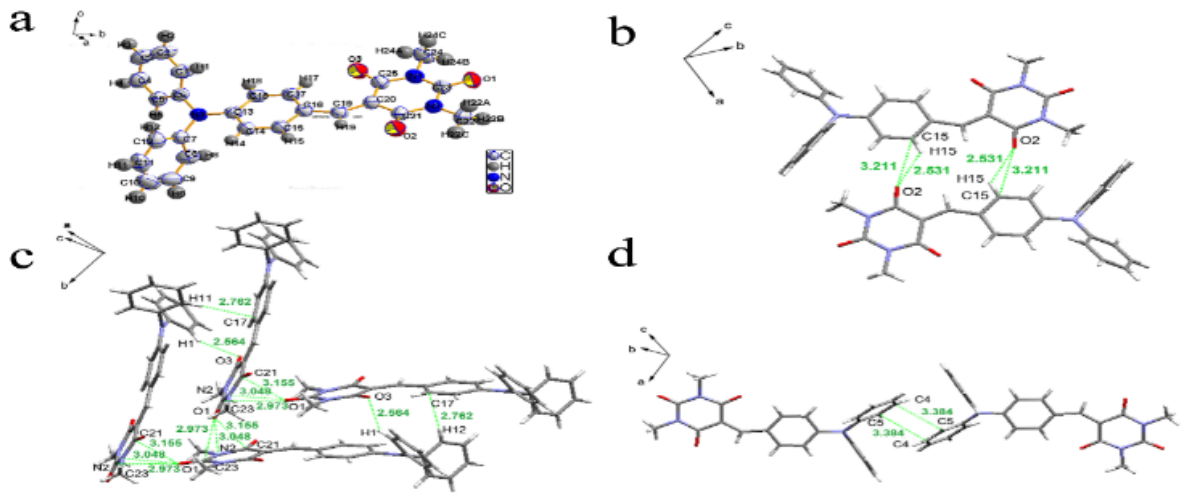

Fig. 10. ORTEP (thermal ellipsoids at 50% probability level) diagram (a), one-dimensional structure (b), herringbone stack structure (c), and π-π interaction (d) of PB-2. (Adopted from Royal Society of Chemistry with permission for reference 4).

3.4 Detection of nitroaromatic explosives

As shown in Fig. 11, fluorescence of PB-3 (f_w = 90%) did not change within 30 minutes under continuous UV irradiation, while the fluorescence of PB-1 and PB-2 decreased remarkably in f_w = 90%. These results means that PB-3 (f_w = 90%) has excellent photo-stability and could be used for explosive detection.

The ^{1}H NMR spectra of PB-1, PB-2 and PB-3 were measured before and after being irradiated for 24 hours under the UV lamp (365 nm). The results can be found in S17-S19 in the supporting information. It is obvious from Fig. S17 that N-H peak at 11.0 ppm on the barbituric acid of PB-1 disappears after being irradiated by UV, accompanied by a new peak near 3.5 ppm which could be ascribe to the peak of O-H. This change of ^{1}H NMR spectra is in agreement with the fact that PB-1 undergoes tautomerization from keto to enol structure, which is responsible for great decrease of fluorescence intensity (by 95% in 30 minutes). For PB-2, the chemical shifts of the hydrogen atom in the triphenylamine moiety remained unchanged after being irradiated, while those in both the methyls and vinyls around the barbituric acid shifted to the high field (Fig. S18). This spectral changes meant the photo reaction occurred around barbituric acid group, which leading to the severe photobleaching of PB--2 that the fluorescence intensity decreased by 95% in 30 minutes. Unfortunately, the reason for the photo reaction has not yet been clarified. For PB-3, there was almost no change in ^{1}H NMR spectra after being irradiated for 24 hours under the UV lamp (365 nm)

(Fig. S19), indicating that its chemical structure did not change, this phenomenon well explained the great photo-stability of PB-3.

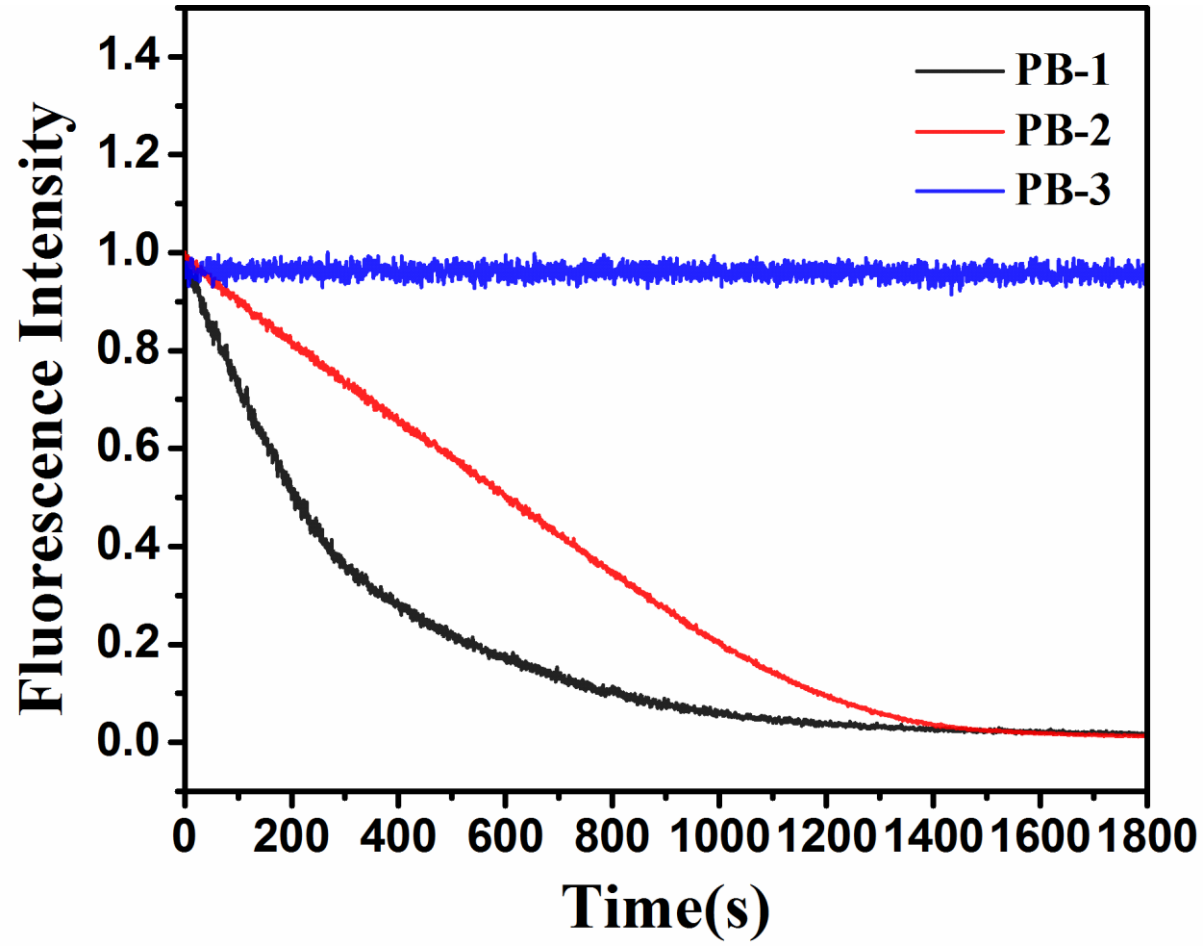

Fig. 11. Light stability of PB-1, PB-2, PB-3 in f_w = 90%.

The fluorescence quenching of PB-3 (f_w = 90%) nano-aggregates was tested in the presence of 2,4-dinitrotoluene (DNT), 2,4,6-Trinitrotoluene (TNT) and 2,4,6-trinitrophenol (PA) with equivalents of nitroaromatics (0.8×10^{-2} g/L). As shown in Fig. 12, PA, TNT or DNT were gradually added to PB-3 (f_w = 90%) solution, and the fluorescence gradually weakened, but we could see that the dripping of PA led to the fastest fluorescence reduction. The fluorescence intensity of quenching at different concentrations (0–1.6×10^{-2} g/L) was recorded, and the Stern-Volmer curve was obtained. It was found that the quenching curve of nitroaromatic compounds (0–0.8×10^{-2} g/L) at low concentration was linear. As shown in Fig. 13, the quenching constants (K_{SV}) of various nitroaromatic compounds were obtained by fitting the data [27]. It can be seen from the figure that the values of K_{SV} of PA, TNT and DNT are 4.1×10^{4}, 1.4×10^{4} and 2.0×10^{3} M^{-1}, respectively, when the concentration range of

nitroaromatics are matched (0–0.8×10^{-2} g/L). It can be seen that the K_{SV} of PA is much higher than those of TNT and DNT.

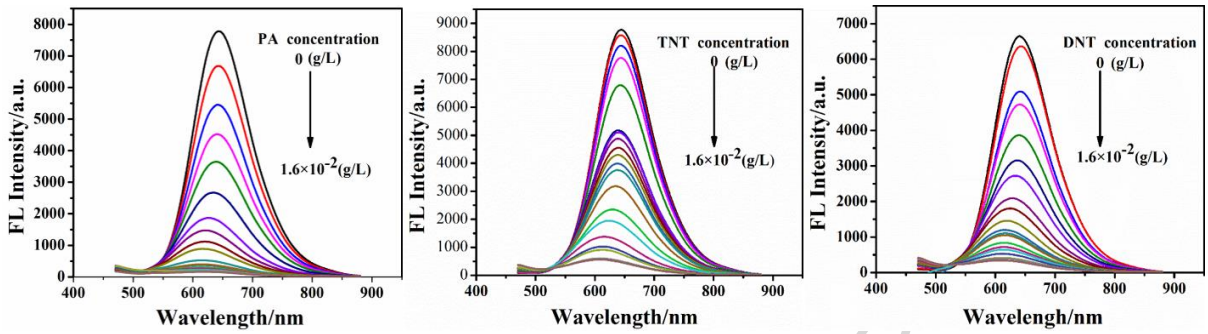

Fig. 12. PB-3 vs. PA, DNT, and TNT quenching fluorescence spectra.

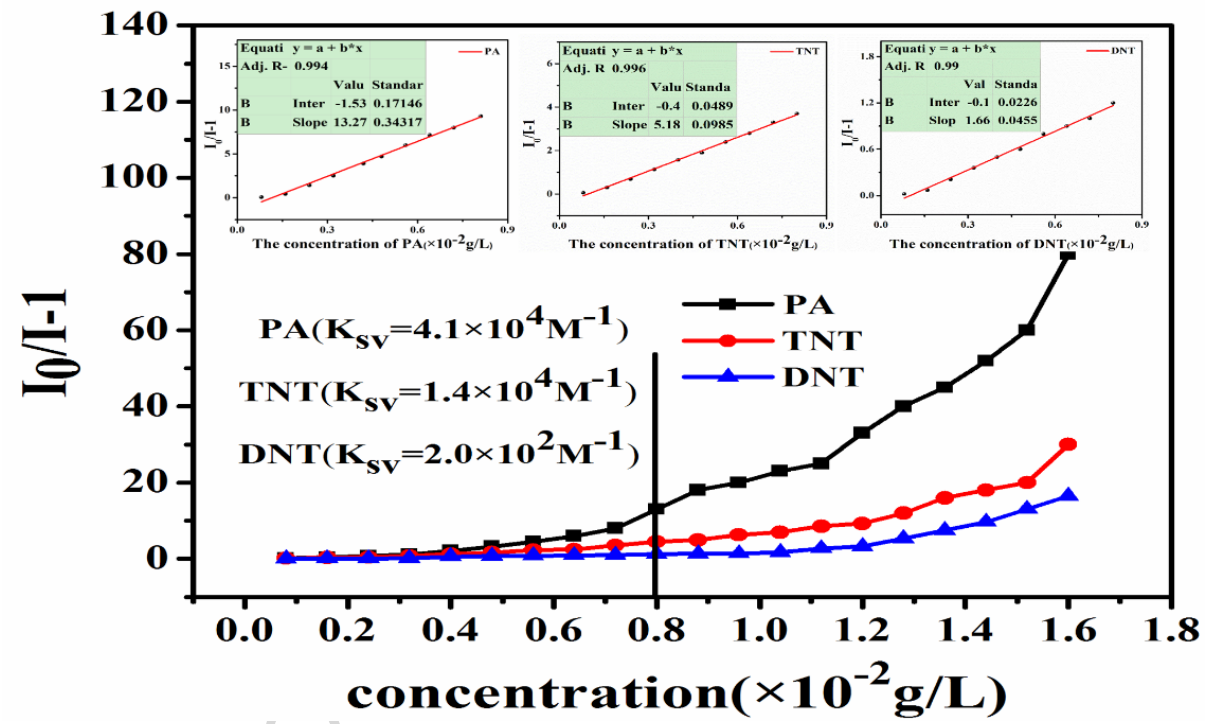

Fig. 13. Fluorescence quenching Stern-Volmer curves of PB-3 with PA, TNT and DNT.

Selectivity is a key criterion for the practicality of sensing materials. In order to test the selectivity of PB-2, PA, TNT, DNT, 1,4-benzoquinone (BQ), chlorobenzene, benzenesulfonic acid, phenol and methanol are used as organic analytes, and meanwhile HCl and KOH as inorganic interferences were studied (Fig. 14). As show in Fig. 14, PA displayed the highest fluorescence quenching efficiency ((1-I/I_0) ×100%) of 90%, and the quenching efficiencies of TNT and DNT with nitro groups were 60% and 50%, respectively. However, there almost no reaction of other compounds. Obviously, PB-3 has better selectivity for PA, TNT and DNT.

The limit of detection (LOD) of PB-3 in THF-H_2O mixture (1: 9 v/v) for PA is 2.4 μM, which can be obtained by the equation LOD = $3S/K_{sv}$, where S is the standard deviation of 15 measurements of blank samples and K_{sv} is known from above. [28, 29].

By analyzing the literatures on fluorescence sensors for NACs, it was found that the K_{sv} of most of the sensing materials concentrates on the order of magnitude of $10^{-4}M^{-1}$ [30-35]. This means that PB-3 exhibited comparable K_{sv} with most of the reported sensing materials. Additionally, PB-3 exhibits outstanding photo-stability among the reported ones, which is an important property for a fluorescent sensor.

Water from different resources (Yellow River water, tap water, and pond water spiked) was tested to see any effect on fluorescence quenching. The fluorescence quenching of PB-3 (f_w = 90%) nano-aggregates was tested in the presence of PA with equivalents of nitroaromatics (0.8×10^{-2} g/L). As shown in Fig. 15, it is obvious that the quenching effect is the same in different water environments, so it can be concluded that water from different sources does not affect the quenching behavior.

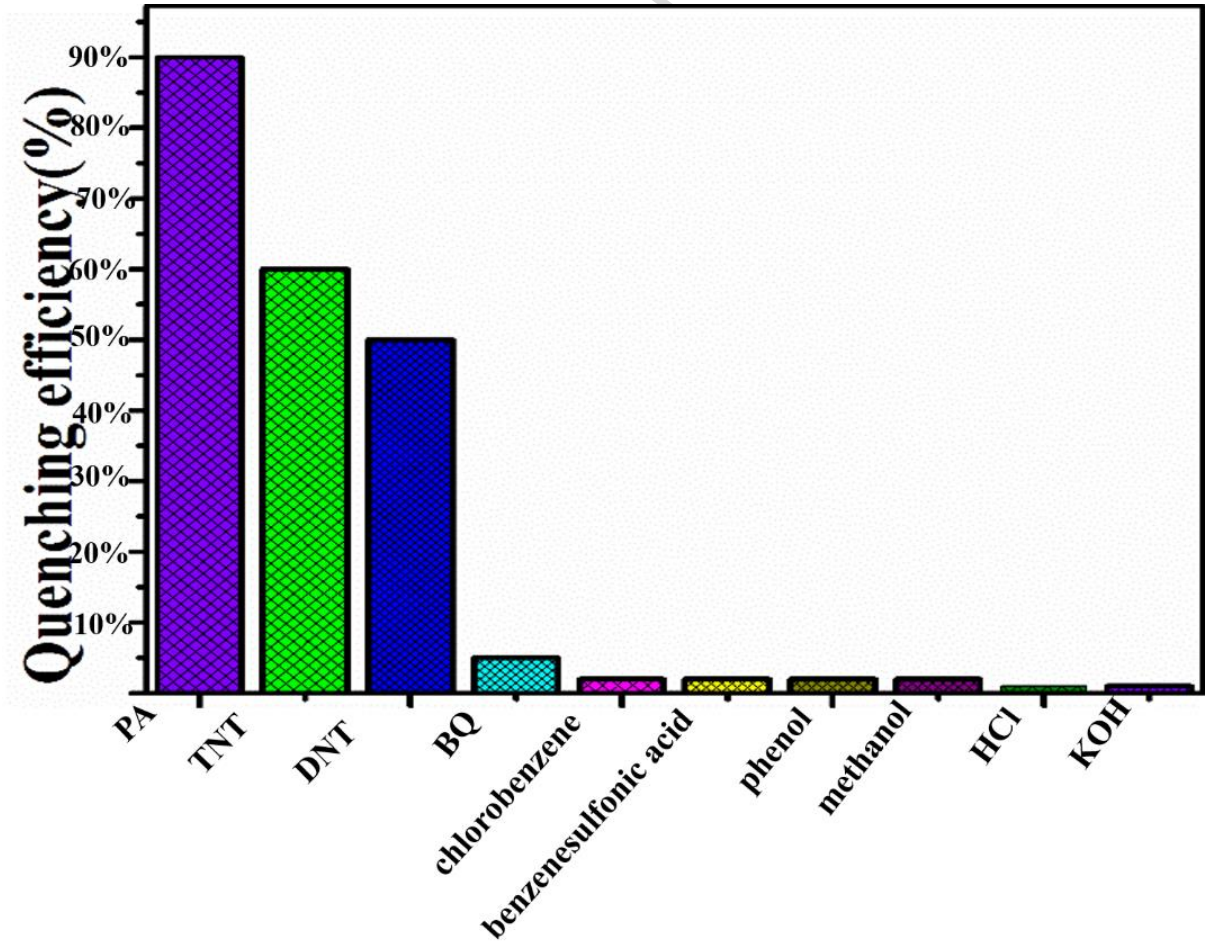

Fig. 14. Quenching efficiencies of PB-3 for (0.8×10^{-2} g/L) NACs and various interferents in

THF-H_2O mixture (1:9 v/v) at room temperature.

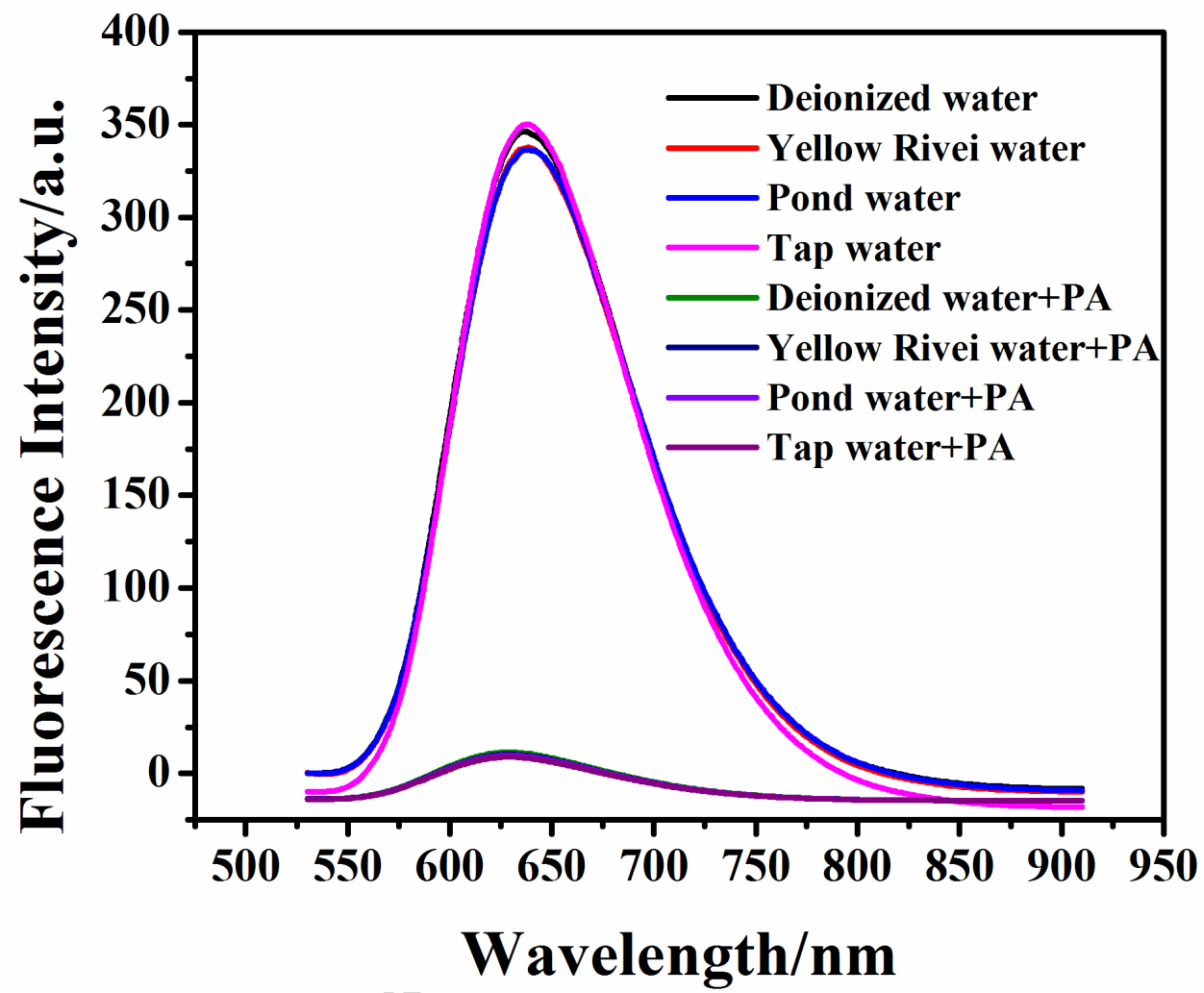

Fig. 15. Fluorescence response of PB-3 (THF:H_2O mixture (1:9 v/v)) toward PA in different water resources.

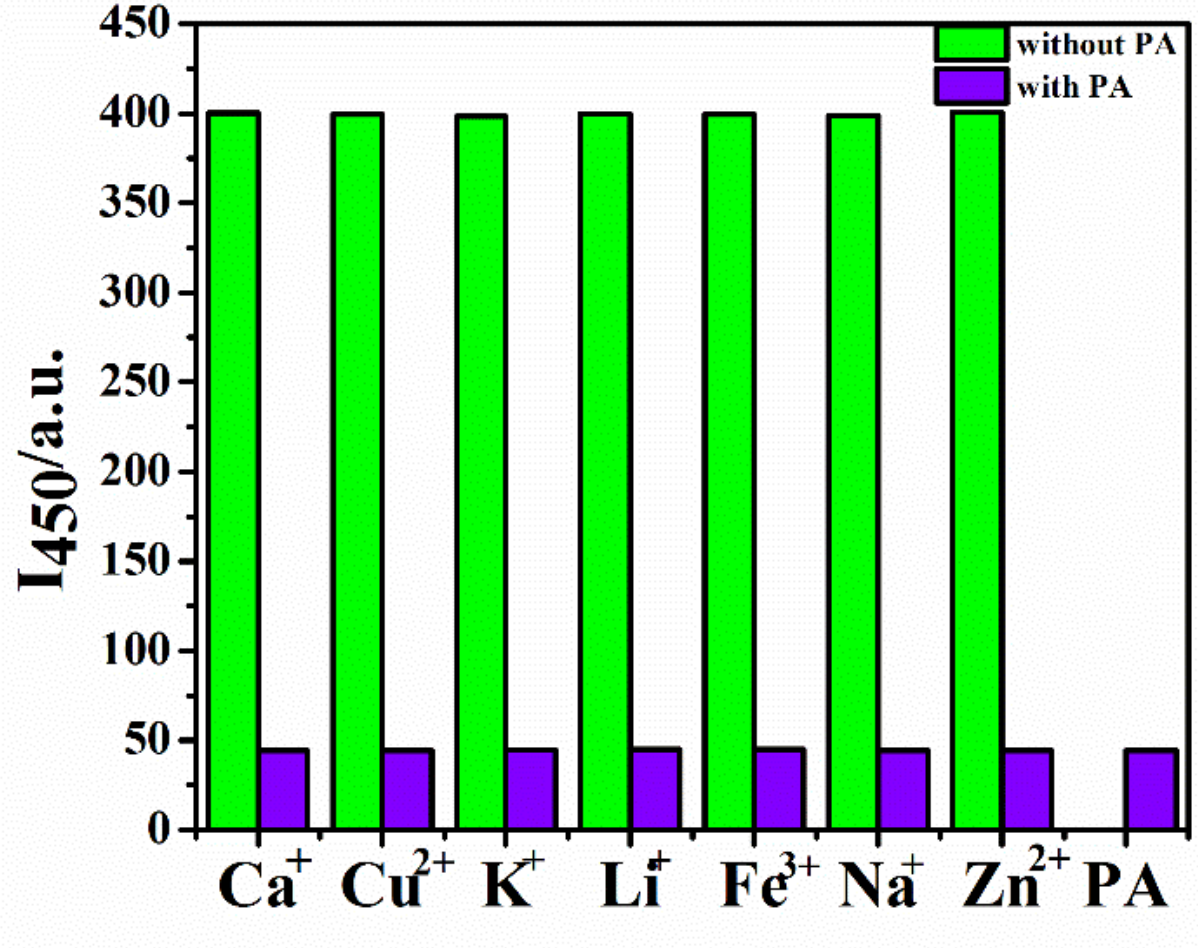

Fig. 16. Column diagrams of fluorescence detection of PA performed in the presence of different metal ions. Green bars: metal ion solution (c = 10^{-5} M). Purple bars: metal ion solution with PA (c = 10^{-4} M) (PB-3, f_w = 90%) + metal ion + PA).

Simultaneously, there may be a lower concentration of metal ions in different waters, which may affect the detection of PA. Therefore, fluorescence detection of PA was performed in the presence of different metal ions. As shown in Fig. 16, the presence of metal ions does not affect the detection of PA.

The availability of solid-state sensor equipment is critical for practical explosive detection. To achieve this goal, we prepared the test paper by soaking Whatman filter paper in PB-3 (f_w = 90%) (10^{-4} M) solution and then dried it in air stream. The first is the vapor mode test. We placed the fluorescent test paper on a glass vial containing solid PA (0.2 g) for 5 minutes. The circular area of the test strip was exposed to PA vapor. It can be seen that the PL of the aggregate is obviously quenched in the exposed area as shown in Fig. 17A. Then, the

solution state was tested. The test paper were immersed into pure THF (as reference) and a solution of PA in THF (10^{-4} M). As shown in Fig. 17B, the fluorescence of the test paper quenched completely when it was immersed in PA/THF (Fig. 17B.e). On the contrary, there is no obvious PL quenching phenomenon in the reference paper immersed in pure THF (Fig. 17B.d). These experimental results indicate that PB-3 can be used to prepare the sensitive sensor for detecting nitroaromatic explosive.

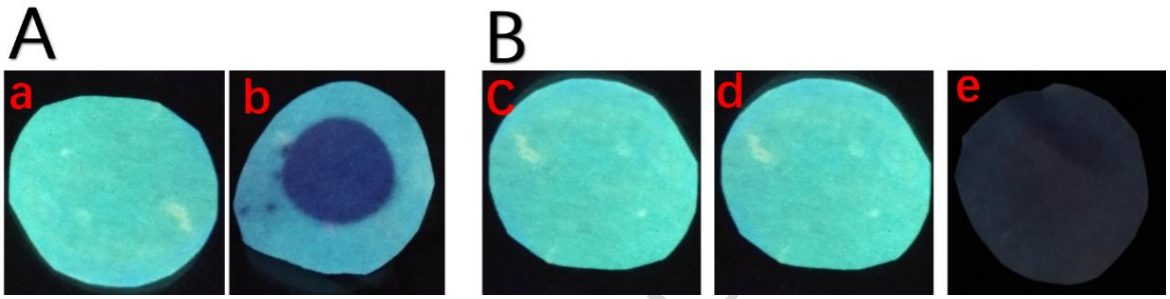

Fig. 17. Paper test. (A) Gas phase mode detection of PA: before (a) and after (b) the test strip is placed on top of a glass bottle containing solid PA for 5 minutes; (B) Solution mode.

3.4.1 Sensing mechanism

The two mechanisms of PB-3 quenching may be Förster resonance energy transfer (FRET) and photoinduced electron transfer (PET) [36-38]. In order to verify whether the quenching of PB-3 is due to the presence of FRET, different nitroaromatics (NACs) absorption spectra and PB-3 emission spectra were tested. As shown in Fig. 18, the absorption spectra of NACs (PA, TNT and DNT) do not overlap with the emission spectra of PB-3 (as a prerequisite for Forster-type energy transfer), and the results suggest that FRET mechanism is negligible.

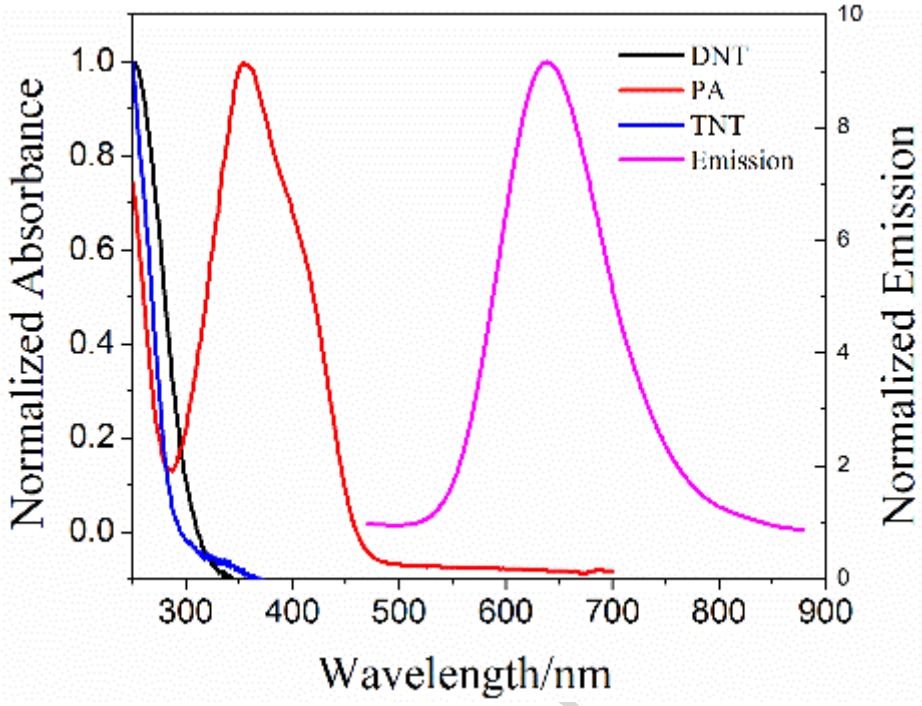

Fig. 18. Absorption and emission spectra of TNT, DNT, PA and PB-3.

Theoretical calculations were made on the basis of B3LYP/6-31g (d) to determine the LUMO and HOMO energies of PB-3 and NACs. As shown in Fig. 8, the optimized geometry of PB-3 exhibits a distorted conformation which can be free to rotate in a pure solution, thus energy consumption due to non-radiative transitions, so its emission intensity is weak in pure solution. The calculated results show that the electron densities of HOMO is located in the triphenylamine, whereas the electron densities of LUMO is confined to barbituric acid group (Fig. 19). These indicate that charge transfer from the triphenylamine group to the barbituric acid group occurs in the excited state of PB-3. When the excited PB-3 is exposed to NACs, the excited electrons are transferred from the LUMO of PB-3 to the LUMO of NACs. The main driving force of PET is the difference between the LUMO value of the tested compound and the NACs. The driving forces of PA, TNT and DNT were 1.194, 0.627 and 0.176 eV, respectively (Fig. 19). Compared with other NACs, PA has the most significant driving force (1.194 eV) in PET mechanism, so PB-3 shows special selectivity for PA in three NACs [39].

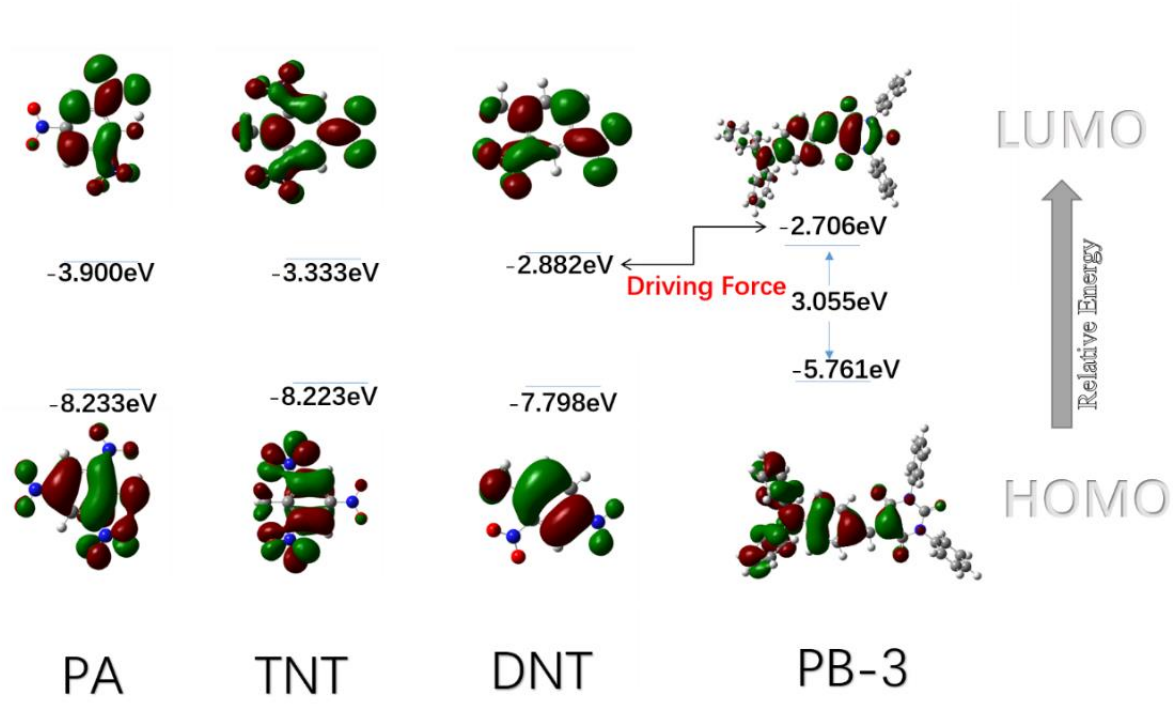

Fig. 19. Energy levels, energy gaps and electron cloud distributions of the HOMO and LUMO of PA, TNT, DNT and PB-3 calculated by the B3LYP/6-325 31G (d) program.

4 Conclusions

Three D-π-A type barbituric derivatives were synthesized and the AIE property related to the molecular structure of barbituric derivatives. In comparison with PB-1 and -2), PB-3 showed strikingly fluorescence stability at high water fractions THF/H_2O = 1:9 (f_w = 90%), therefore further for great sensitivity detection as a prototype of the nitroaromatic analyte of PA. Solid phase paper test based on PB-3 was also showed great sensitivity toward PA both in the vapor and solutions.

Acknowledgements

This work was financially supported by the Natural Science Foundation of Shandong province (ZR2018MB025), Key R&D Program Projects of Shandong province (2017GGX202001) and the Funds for Research Leader in Jinan （2018GXRC028）.

References

[1] Luo J, Xie Z, Lam J W Y, et al. Aggregation-induced emission of 1-methyl-1,2,3,4,5-pentaphenylsilole[J]. Chemical Communications, 2001(18):1740-1741.

[2] Zhao Z, He B, Tang B Z. ChemInform Abstract: Aggregation‐Induced Emission of Siloles [J]. Cheminform, 2015, 6:5347-5365.

[3] Chen B, Jiang Y, He B, et al. Synthesis, Structure, Photoluminescence, and Electroluminescence of Siloles that Contain Planar Fluorescent Chromophores [J]. Chem Asian J, 2015, 9(10):2937-2945.

[4] Li K, Zhang Y, Qiao B, et al. Facile fabrication of AIE/AIEE-active fluorescent nanoparticles based on barbituric for cell imaging applications[J]. Rsc Advances, 2017, 7(48):30229-30241.

[5] Qian J, Zhu Z, Qin A, et al. High-Order Non-linear Optical Effects in Organic Luminogens with Aggregation‐Induced Emission [J]. Advanced Materials, 2015, 27(14):2332-2339.

[6] Zhang Y, Li D, Li Y, et al. Solvatochromic AIE luminogens as supersensitive water detectors in organic solvents and highly efficient cyanide chemosensors in water [J]. Chemical Science, 2014, 5(7):2710-2716.

[7] Zhang X, Liu M, Yang B, et al. Cross-linkable aggregation induced emission dye based red fluorescent organic nanoparticles and their cell imaging applications[J]. Polymer Chemistry, 2013, 4(19):5060-5064.

[8] Wang C, Ji H, Li M, et al. A highly sensitive and selective fluorescent probe for hypochlorite in pure water with aggregation induced emission characteristics [J]. Faraday Discussions, 2017, 196:427-438.

[9] Misra R, Jadhav T, Dhokale B, et al. Reversible mechanochromism and enhanced AIE in tetraphenylethene substituted phenanthroimidazoles [J]. Chemical Communications, 2014, 50(65):9076-9078.

[10] L i R, Xiao S, Li Y, et al. Polymorphism-dependent and piezochromic luminescence based on molecular packing of a conjugated molecule[J]. Chemical Science, 2014, 5(10):3922-3928.

[11] Germain M E, Knapp M J. Optical explosives detection: from color changes to fluorescence turn-on. [J]. Cheminform, 2009, 38(9):2543-2555.

[12] Gole B, Song W, Lackinger M, et al. Explosives sensing by using electron-rich supramolecular polymers: role of intermolecular hydrogen bonding in significant enhancement of sensitivity. [J]. Chemistry - A European Journal, 2015, 20(42):13662-13680.

[13] Pon S N, Venugopalan S, Senthilkumar N, et al. Voltammetric determination of nitroaromatic and nitramine explosives contamination in soil [J]. Talanta, 2006, 69(3):656-662.

[14] Salinas Y, MartãNez-Mã Ã R, Marcos M D, et al. Optical chemosensors and reagents to detect explosives [J]. Chemical Society Reviews, 2012, 41(3):1261-1296.

[15] Wang D.H, Cui Y.Z, Tao F.R. et al. A novel film of conjugated polymer grafted onto gelatin for detectingnitroaromatics vapor with excellent inhibiting photobleaching.Sensors and Actuators B, 2016, 225,319-326.

[16] NakamaruKatsumi. Synthesis, Luminescence Quantum Yields, and Lifetimes of Trischelated Ruthenium (II) Mixed-ligand Complexes Including 3, 3′-Dimethyl-2, 2′-bipyridyl [J]. Bulletin of the Chemical Society of Japan, 1982, 55(9):2697-2705.

[17] Santra D C, Bera M K, Sukul P K, et al. Charge-Transfer-Induced Fluorescence Quenching of Anthracene Derivatives and Selective Detection of Picric Acid [J]. Chemistry - A European Journal, 2016, 22(6):2012-2019.

[18] J. N. Demasa, G. A. Crosby. Measurement of Photoluminescence Quantum Yields [J]. Chemistry International, 2015, 37(5-6).

[19] P.Y. Gu, C.J. Lu, Z.J. Hu, N.J. Li, T.T. Zhao, Q.F. Xu, et al. The AIEE effect and two-photon absorption (TPA) enhancement induced by polymerization: synthesis of a monomer with ICT and AIE effects and its homopolymer by ATRP and a study of their photophysical properties. Journal of Materials Chemistry C: Materials for Optical and Electronic Devices, 2013, 1(14), 2599-2606.

[20] Thilagar P, Mukherjee S. Molecular Flexibility Tuned Emission in “V” Shaped Naphthalimides: Hg (II) Detection and Aggregation-Induced Emission Enhancement (AIEE) [J]. Chemical Communications, 2013, 49(66):7292-7294.

[21] Fujii K, Iyi N, Sasai R, et al. Preparation of a Novel Luminous Heterogeneous System: Rhodamine/Coumarin/Phyllosilicate Hybrid and Blue Shift in Fluorescence Emission [J] . Chemistry of Materials, 2008, 20(9):2994-3002.

[22] Piton A, K M, Neogra P, Reza J, et al. Benzene Dimer: High-Level Wave Function and Density Functional Theory Calculations [J]. Journal of Chemical Theory and Computation, 2008, 4(11):1829-1834.

[23] Kai L, Xi S, Yi xuan W, et al. D-π-A type Barbituric Derivatives: Aggregation induced emission, mechanofluorochromic and solvatochromic properties [J]. Journal of Luminescence, 2018, 203:50-58.

[24] Dong W, Pina J, Pan Y, et al. Polycarbazoles and polytriphenylamines showing aggregation-induced emission (AIE) and intramolecular charge transfer (ICT) behavior for the optical detection of nitroaromatic compounds [J]. Polymer, 2015, 76:173-181.

[25] S. Vyas, R. Gutzler, J. Nuss, K. Kernab and V. Bettina, Optical gap in herringbone and p-stacked crystals of [1] benzothieno [3, 2-b] benzothiophene and its brominated derivative, Cryst Eng Comm, 2014, 16, 7389–7392.

[26] C. W. Chang, C. J. Bhongale, C. S. Lee, W. K. Huang, C. S. Hsu, W. G. Diau, et al., Relaxation Dynamics and Structural Characterization of Organic Nanobelts with Aggregation-Induced Emission, J. Phys. Chem. C, 2012, 116,15146–15154.

[27] Ma X, Tao F, Zhang Y, et al. Detection of nitroaromatic explosives by a 3D hyperbranched σ–π conjugated polymer based on a POSS scaffold [J]. Journal of Materials Chemistry A, 2017, 5(27).

[28] H. Zhou, J.S. Li, M. H. Chua, H. Yan, B.Z. Tang and J.W. Xu. Poly (acrylate) with a tetraphenylethene pendant with aggregation-induced emission (AIE) characteristics: highly stable AIE-active polymer nanoparticles for effective detection of nitro compounds. Polym. Chem., 5 (2014) 5628-5637.

[29] S. Chemate, Y. Erande, D. Mohbiya and N. Sekar. Acridine derivative as a “turn on” probe for selective detection of picric acid via PET deterrence. RSC Adv., 6 (2016), 84319-84325.

[30] Z.J Luo, B. Liu, S.F. Si, Y.J. Lin, Crystal S.J. Luo, C.J. Pan, C. Zhao and Lei Wang. A fluorescent chemosensor based on nonplanar donor-acceptor structure for highly sensitive and selective detection of picric acid in water. Dyes and Pigments, 143(2017), 463-469.

[31] Ma X, Tao F, Zhang Y, et al.2D hyperbranched conjugated polymer for detecting TNT with excellent exciton migration[J]. Sensors & Actuators B Chemical, 2017, 238:48-57.

[32] C. T. Zhou, X. T. Han, G. F. Liao, et al. A Fluorescent Chemosensor with a Hybridized Local and Charge Transfer Nature and Aggregation Induced Emission Effect for the Detection of Picric Acid [J]. Electro, Physical & Theoretical Chemistry, 2019, 4 (10): 2868-2873.

[33] Qi L, Xiao G, Yan F, Jiao W, You Z, and Tai W, et al. A tripodal supramolecular sensor to successively detect picric acid and CN through guest competitive controlled AIE [J]. New J. Chem., 2019, 43, 2030-2036.

[34] Laxmi Raman Adil, Peddaboodi Gopikrishna, and Parameswar Krishnan Iyer. Receptor-Free Detection of Picric Acid: A New Structural Approach for Designing Aggregation-Induced Emission Probes [J]. ACS Appl. Mater. Interfaces 2018, 10, 32, 27260-27268.

[35]Jian T, Xiao Z, Yen W, et al. Ultrafast construction and biological imaging applications of AIE-active sodium alginate-based fluorescent polymeric nanoparticles through a one-pot microwave-assisted Döbner reaction [J]. 2018.153: 99-105

[36] Mirco Natali, Sebastiano Campagna and Franco Scandola Photoinduced electron transfer across molecular bridges: Electron - and hole-transfer superexchange pathways, Chem. Soc. Rev. 2014, 43:4005-4018.

[37] Kaur M, Mehta S K, Kansal S K. A fluorescent probe based on nitrogen doped graphene quantum dots for turn off sensing of explosive and detrimental water pollutant, TNP in aqueous medium[J]. Spectrochim Acta A Mol Biomol Spectrosc, 2017, 180:37-43.

[38] Yuan L, Lin W, Zheng K, et al. FRET-based small-molecule fluorescent probes: rational design and bioimaging applications [J]. Acc Chem Res, 2013, 46(7):1462-1473.

[39] Dong W, Fei T, Palmacando A, et al. Aggregation induced emission and amplified explosive detection of tetraphenylethylene-substituted polycarbazoles [J]. Polymer Chemistry, 2014, 5(13):4048-4053.

Detection of Nitroaromatics Based on Aggregation Induced Emission of Barbituric Acid Derivatives

Han-Jun Zhang, Yan Tian, Fu-rong Tao, William Yu, Kai-Yue You, Lin-Rui Zhou, Xi Su, Tian-duo Li, Yue-Zhi Cui*

School of Chemical and Pharmaceutical Engineering, Qilu University of Technology, Jinan 250353, P. R. China.

Tel: +86 531 89631208; Fax: +86 531 89631760;
E-mail address: yuezhicui@163.com

Highlights:

- We founded that the aggregation induced fluorescence (AIE) properties were affected by the different substituents on barbituric acid. With the molecular volume increasing, the AIE effect decreased.
- We designed and synthetic synthesized barbituric derivatives fluorescence sensors, which can generate aggregates in high water content and can thus be used for the detection of nitroaromatics in aqueous media We founded that the alkyl substituents play important role in forming aggregates of the compounds.

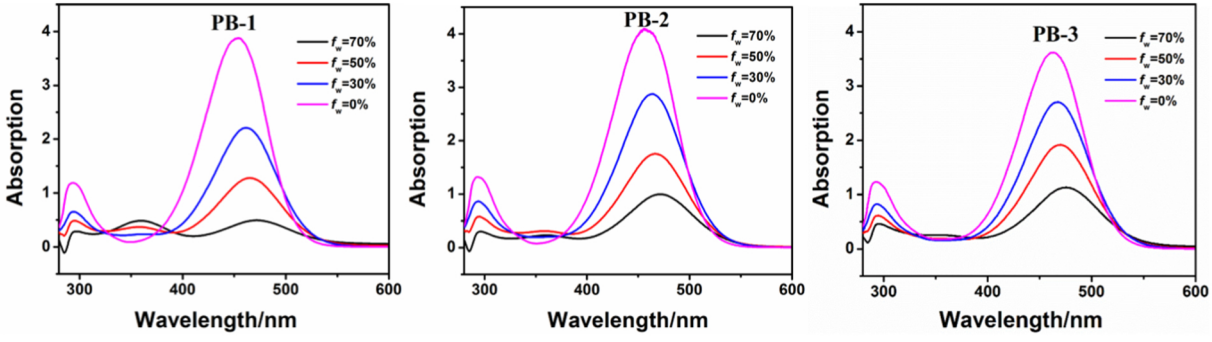
PB-1
PB-2
PB-3
Absorption
Wavelength/nm
f_w=70%
f_w=50%
f_w=30%
f_w=0%
0
1
2
3
4
300
400
500
600

Figure 1

Keto-Enol Tautomerization

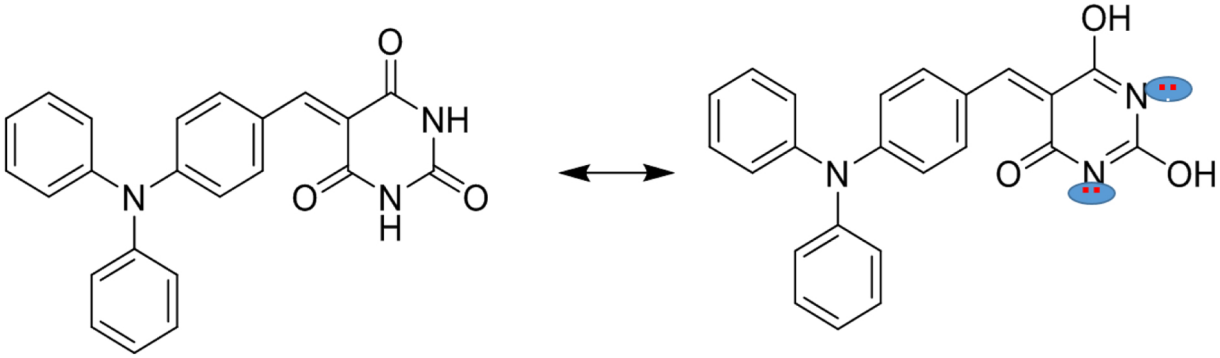

Figure 2

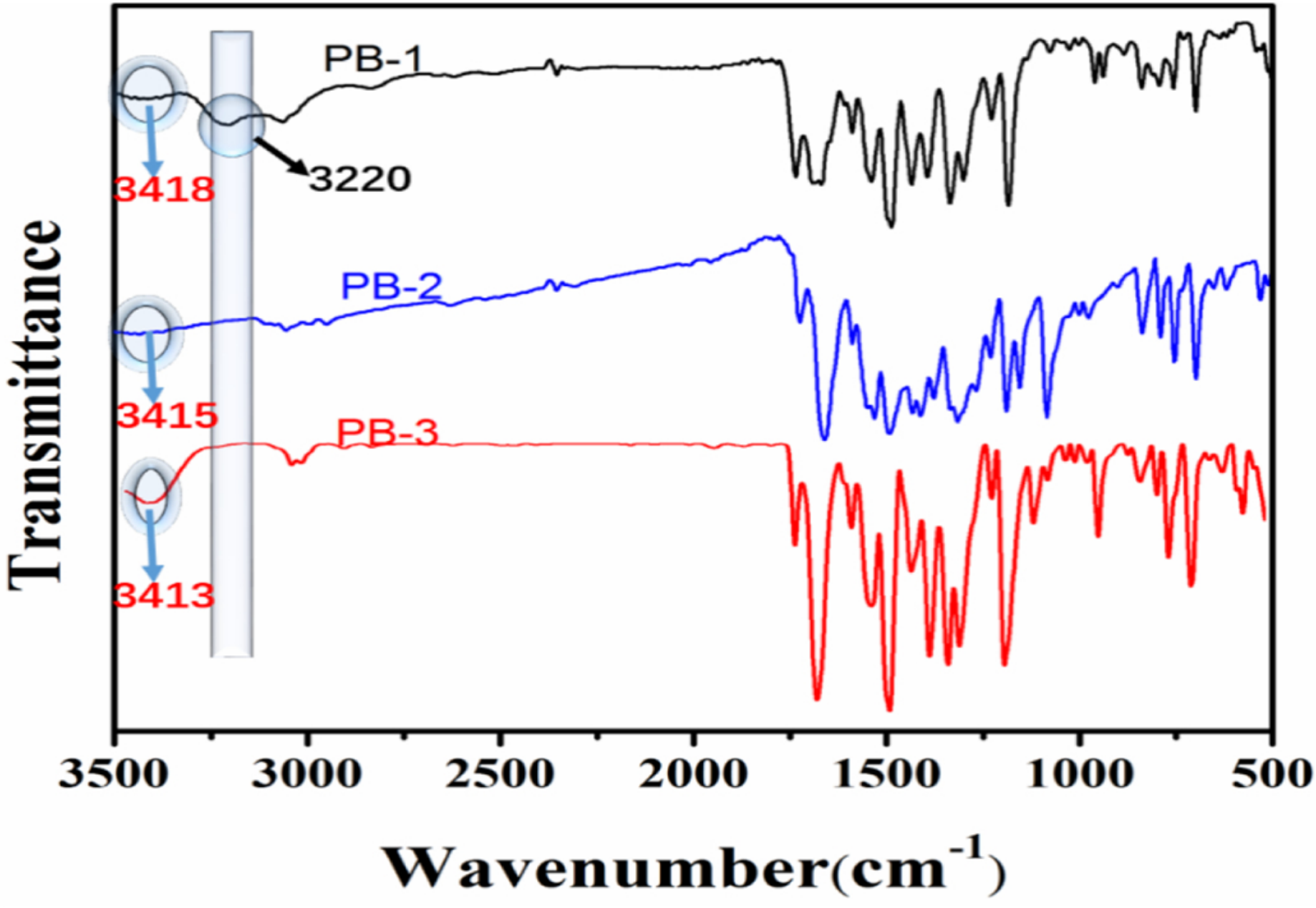
PB-1
3418
3220
PB-2
3415
PB-3
3413
Transmittance
3500
3000
2500
2000
1500
1000
500
Wavenumber(cm-1)

Figure 3


PB-1
solution
powder
PB-2
solution
power
crystal
PB-3
solution
powder

Figure 4

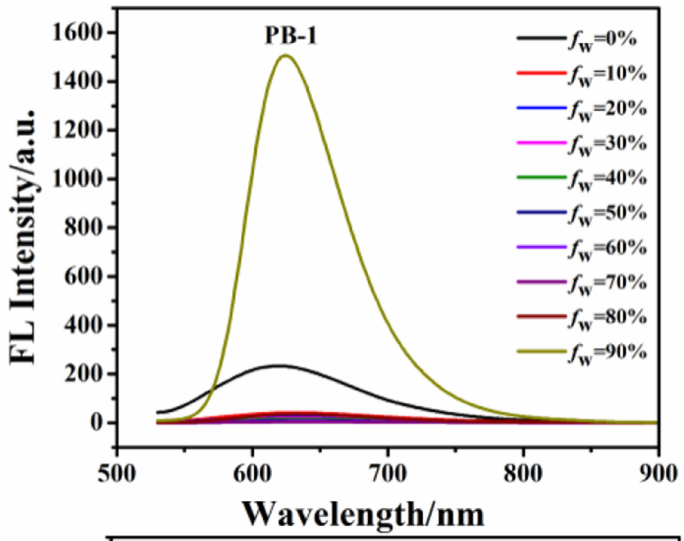
PB-1
FL Intensity/a.u.
Wavelength/nm
f_w=0%
f_w=10%
f_w=20%
f_w=30%
f_w=40%
f_w=50%
f_w=60%
f_w=70%
f_w=80%
f_w=90%

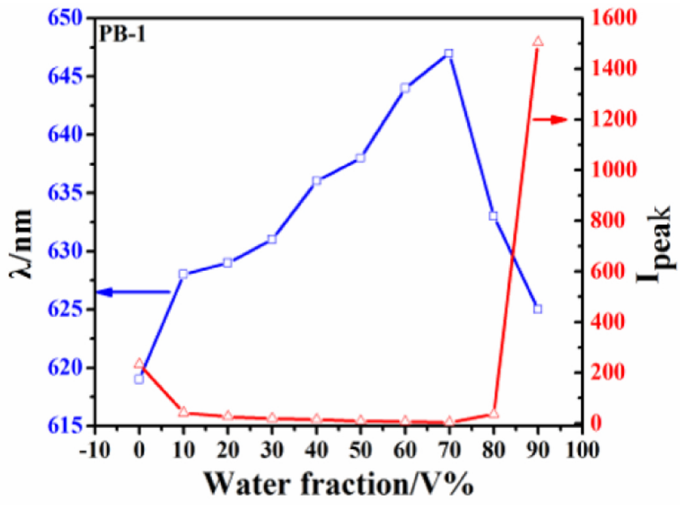
PB-1
λ/nm
I_{peak}
Water fraction/V%

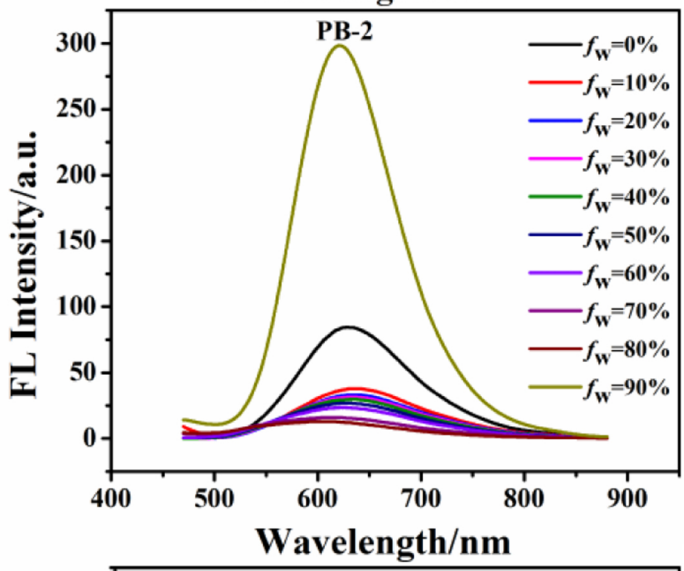
PB-2
FL Intensity/a.u.
Wavelength/nm
f_w=0%
f_w=10%
f_w=20%
f_w=30%
f_w=40%
f_w=50%
f_w=60%
f_w=70%
f_w=80%
f_w=90%

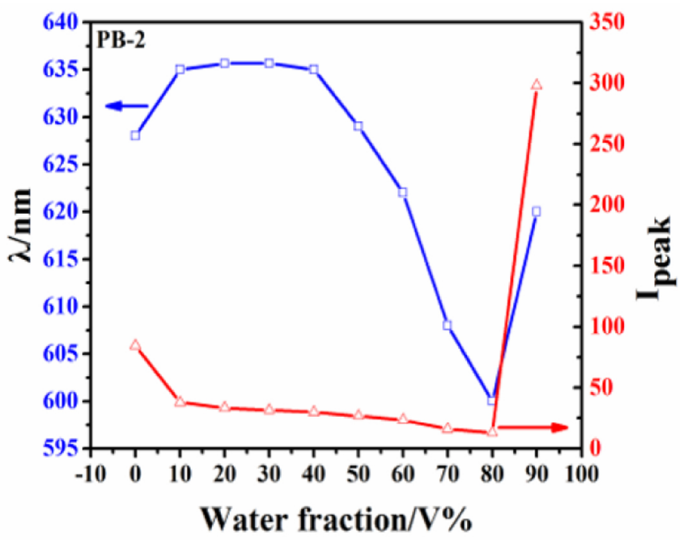
PB-2
λ/nm
I_{peak}
Water fraction/V%

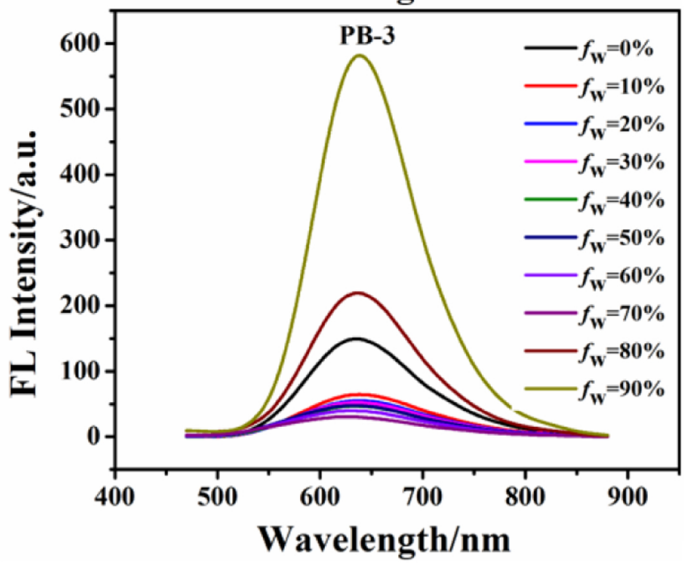
PB-3
FL Intensity/a.u.
Wavelength/nm
f_w=0%
f_w=10%
f_w=20%
f_w=30%
f_w=40%
f_w=50%
f_w=60%
f_w=70%
f_w=80%
f_w=90%

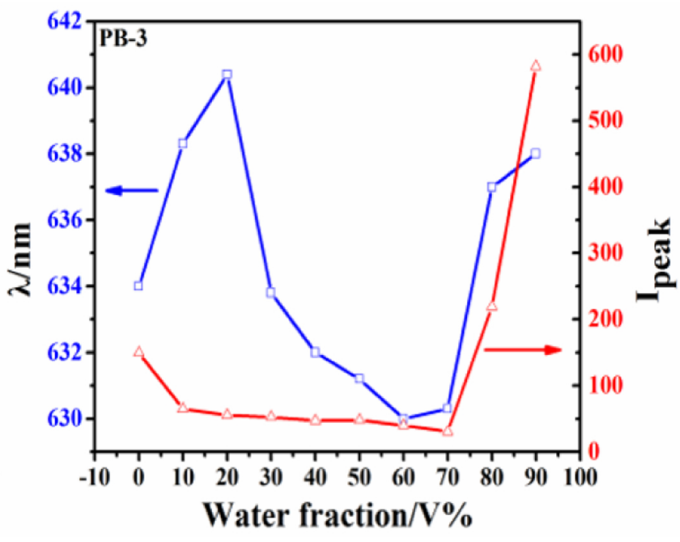
PB-3
λ/nm
I_{peak}
Water fraction/V%

Figure 5

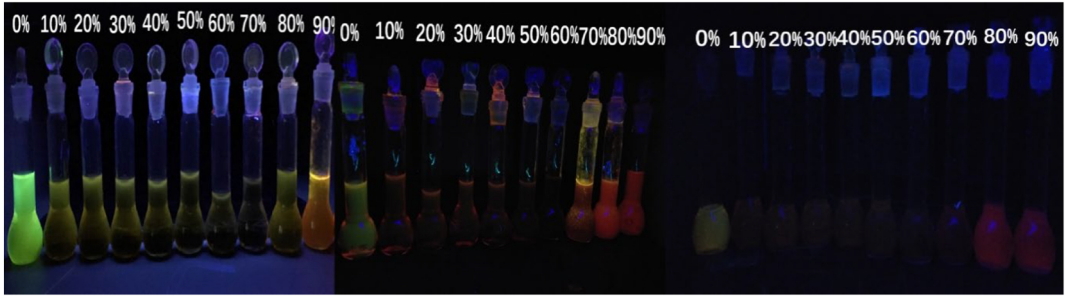
0% 10% 20% 30% 40% 50% 60% 70% 80% 90%
0% 10% 20% 30% 40% 50% 60% 70% 80% 90%
0% 10% 20% 30% 40% 50% 60% 70% 80% 90%

Figure 6

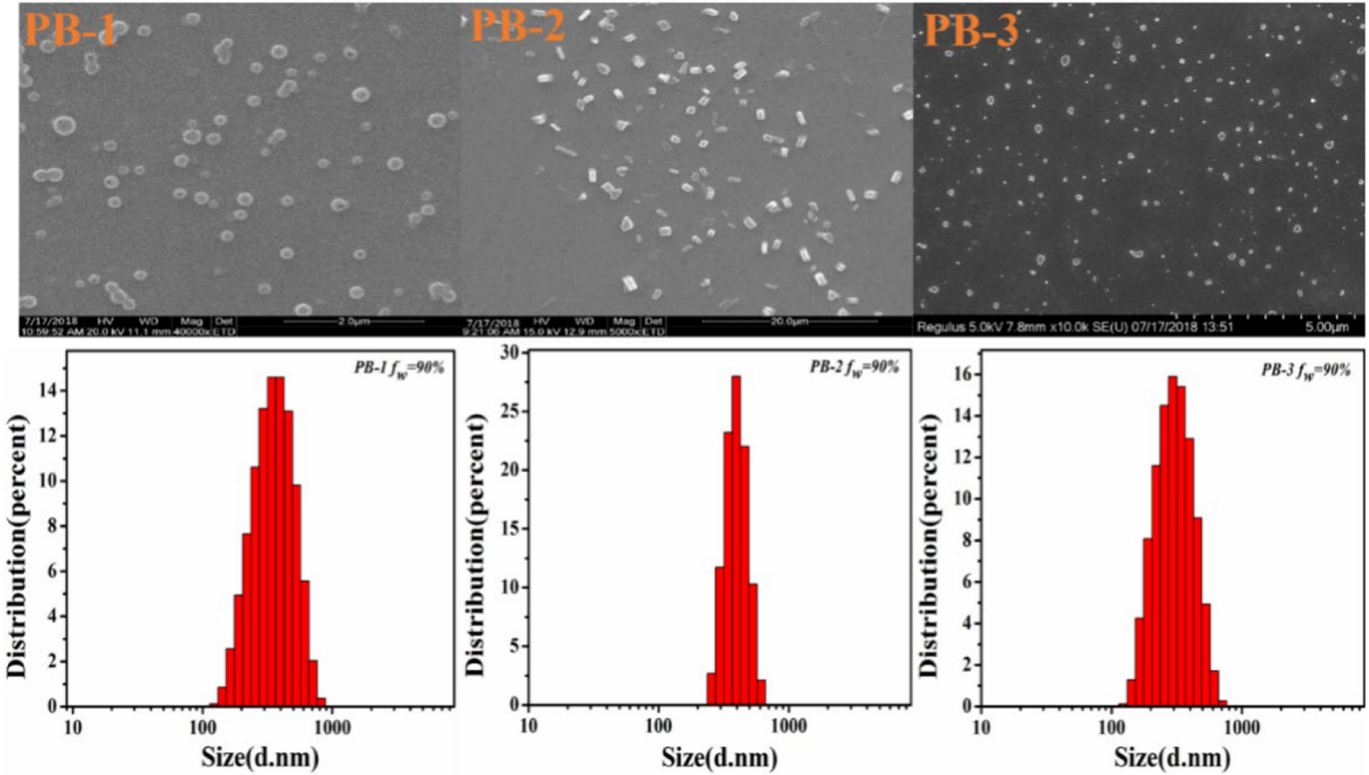
PB-1
PB-2
PB-3
PB-1 f_w=90%
PB-2 f_w=90%
PB-3 f_w=90%
Distribution(percent)
Size(d.nm)

Figure 7

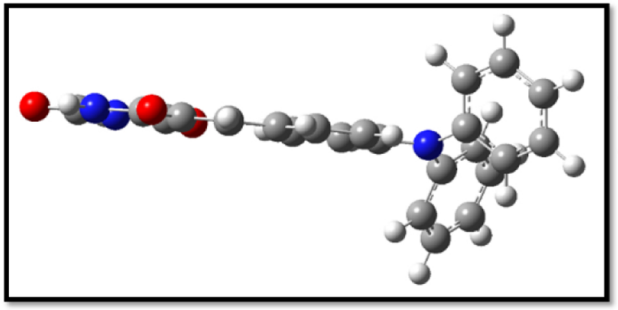

PB-1

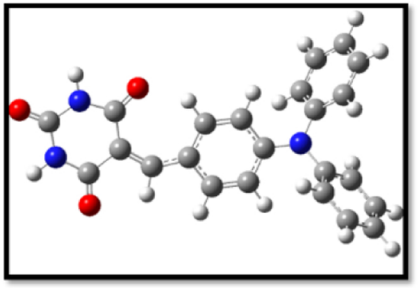

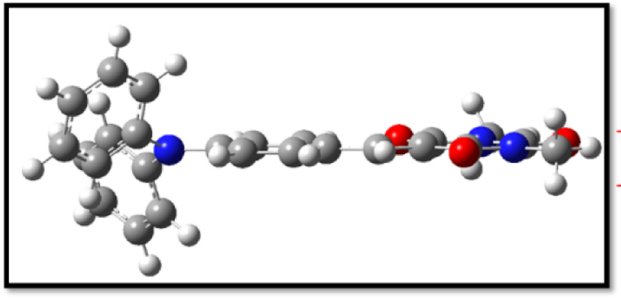

PB-2

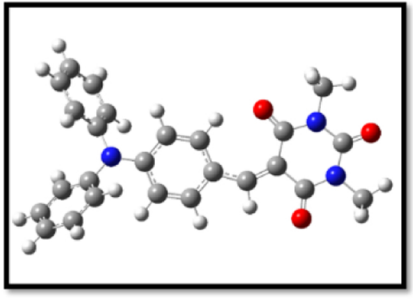

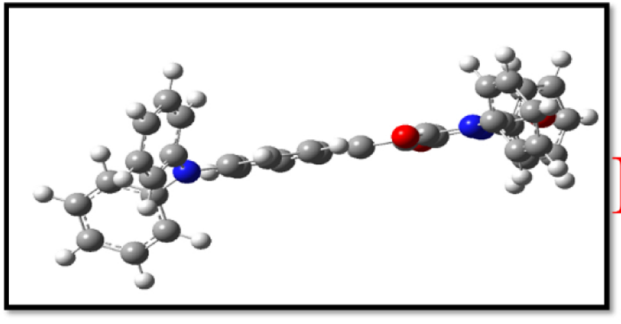

PB-3

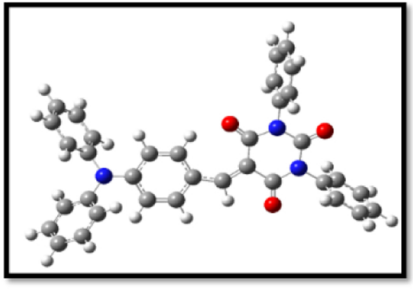

Figure 8

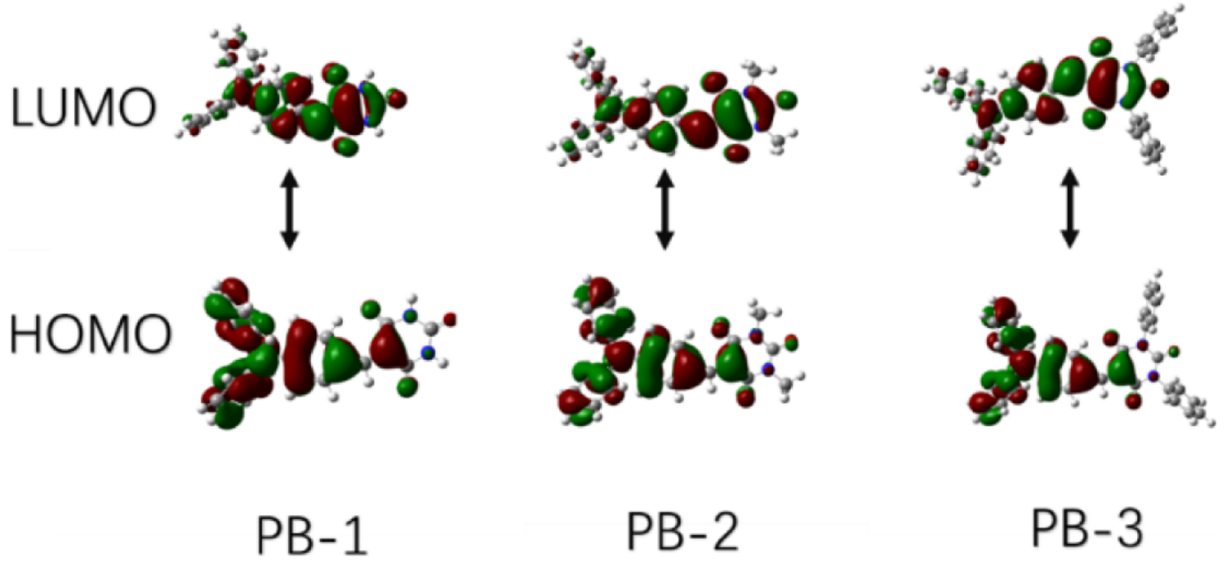

Figure 9

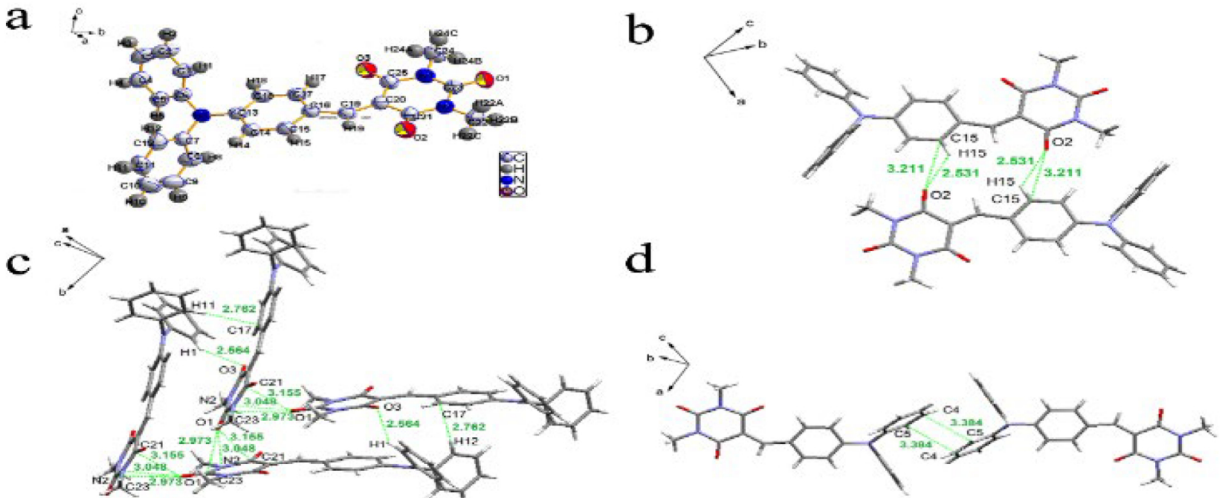
a
b
c
d
C15
H15
O2
3.211
2.531
2.531
3.211
H15
C15
O2
H11
2.762
C17
H1
2.564
O3
C21
3.155
3.048
N2
O1
C23
2.973
O1
O3
C17
2.564
2.762
H11
H12
C21
3.155
2.973
3.765
3.048
N2
C21
3.048
N2
2.973
O1
C23
C4
3.384
C5
C5
3.384
C4

Figure 10

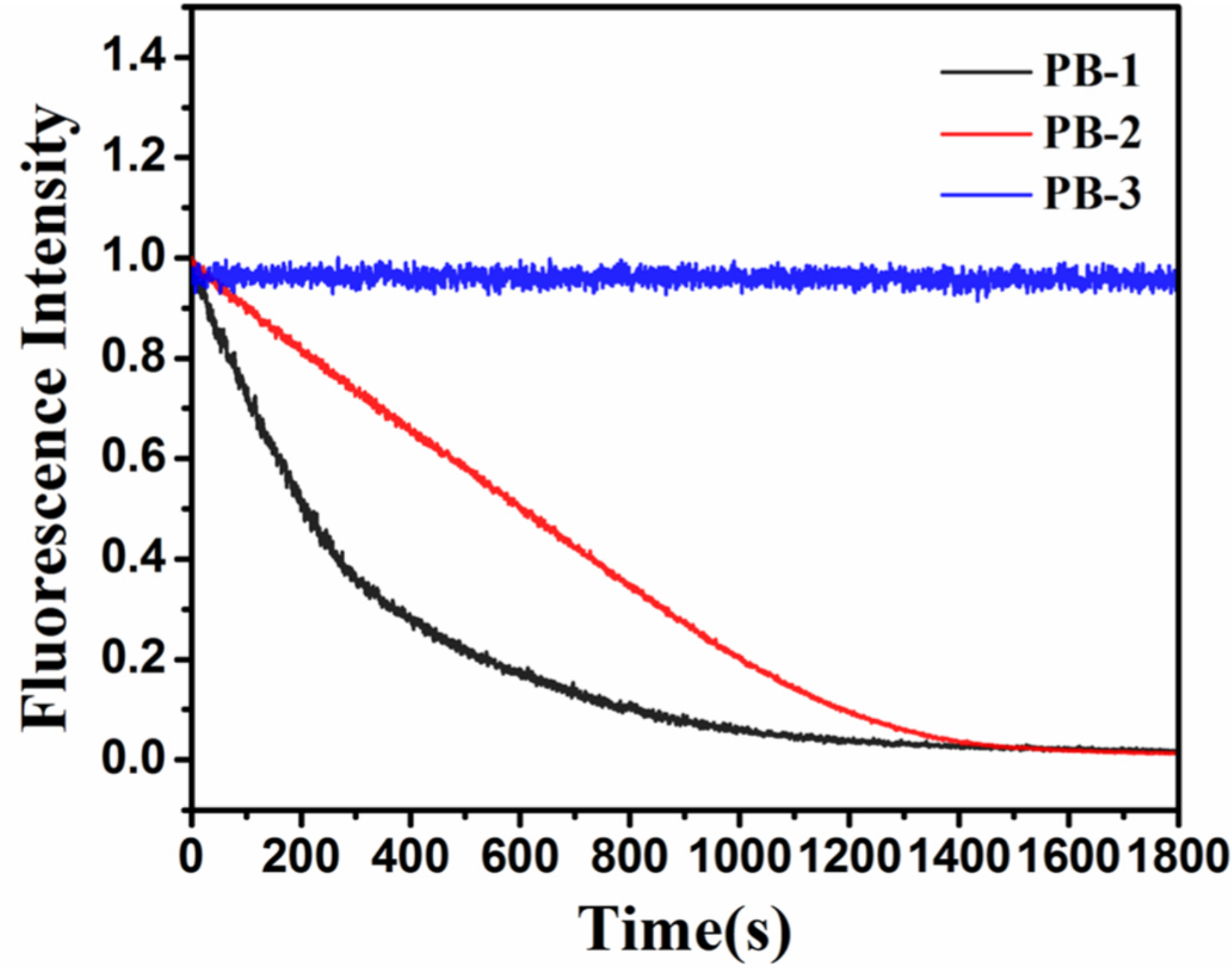
PB-1
PB-2
PB-3
Fluorescence Intensity
1.4
1.2
1.0
0.8
0.6
0.4
0.2
0.0
0
200
400
600
800
1000
1200
1400
1600
1800
Time(s)

Figure 11

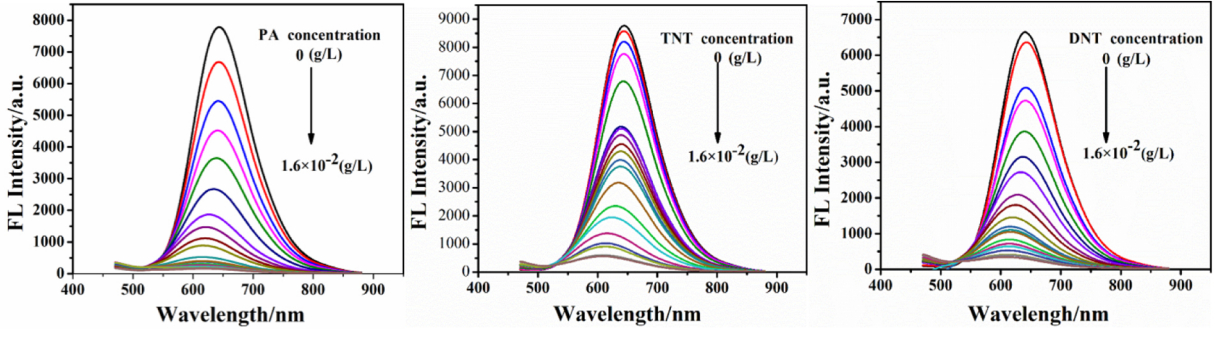
PA concentration
0 (g/L)
1.6×10-2(g/L)
FL Intensity/a.u.
Wavelength/nm
TNT concentration
0 (g/L)
1.6×10-2(g/L)
FL Intensity/a.u.
Wavelength/nm
DNT concentration
0 (g/L)
1.6×10-2(g/L)
FL Intensity/a.u.
Wavelength/nm

Figure 12

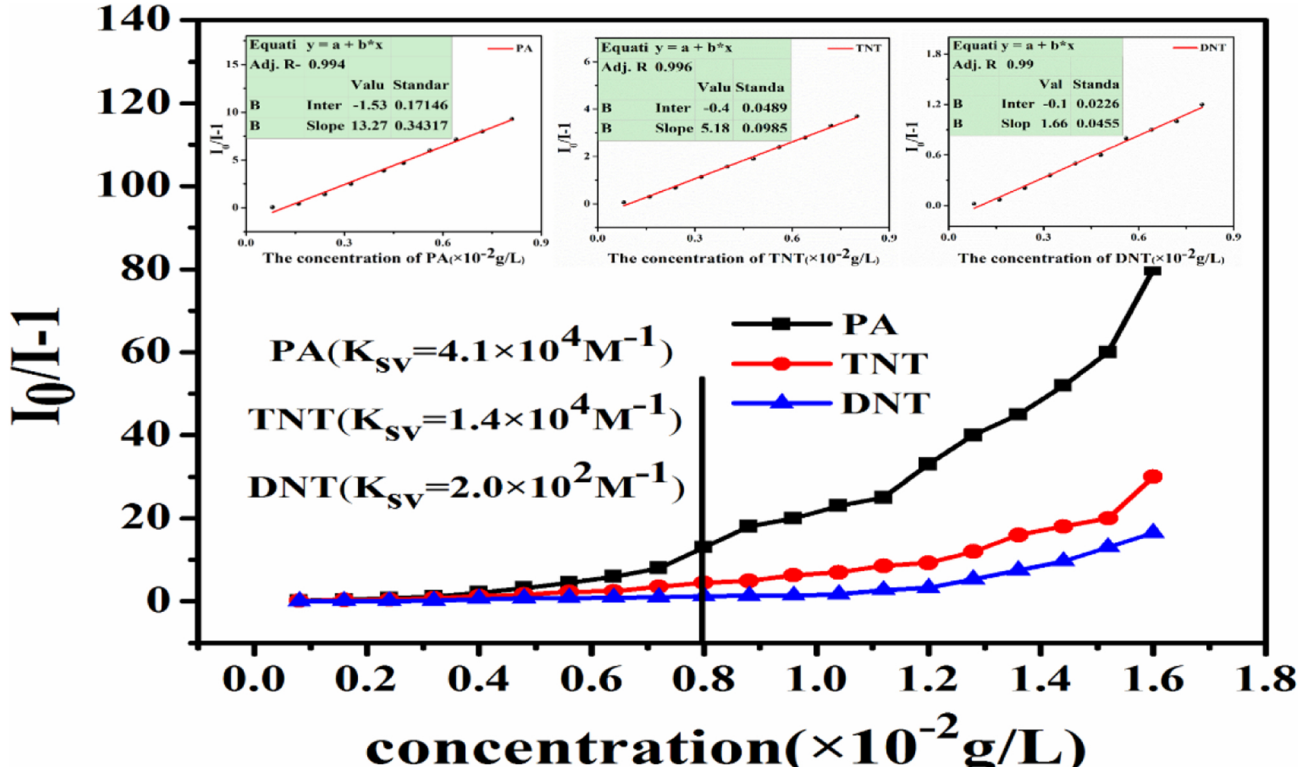
Equati y = a + b*x
Adj. R- 0.994
Valu Standar
B Inter -1.53 0.17146
B Slope 13.27 0.34317
PA
The concentration of PA(×10-2g/L)
Equati y = a + b*x
Adj. R 0.996
Valu Standa
B Inter -0.4 0.0489
B Slope 5.18 0.0985
TNT
The concentration of TNT(×10-2g/L)
Equati y = a + b*x
Adj. R 0.99
Val Standa
B Inter -0.1 0.0226
B Slop 1.66 0.0455
DNT
The concentration of DNT(×10-2g/L)
I0/I-1
PA(KSV=4.1×10^4M^-1)
TNT(KSV=1.4×10^4M^-1)
DNT(KSV=2.0×10^2M^-1)
PA
TNT
DNT
concentration(×10-2g/L)

Figure 13

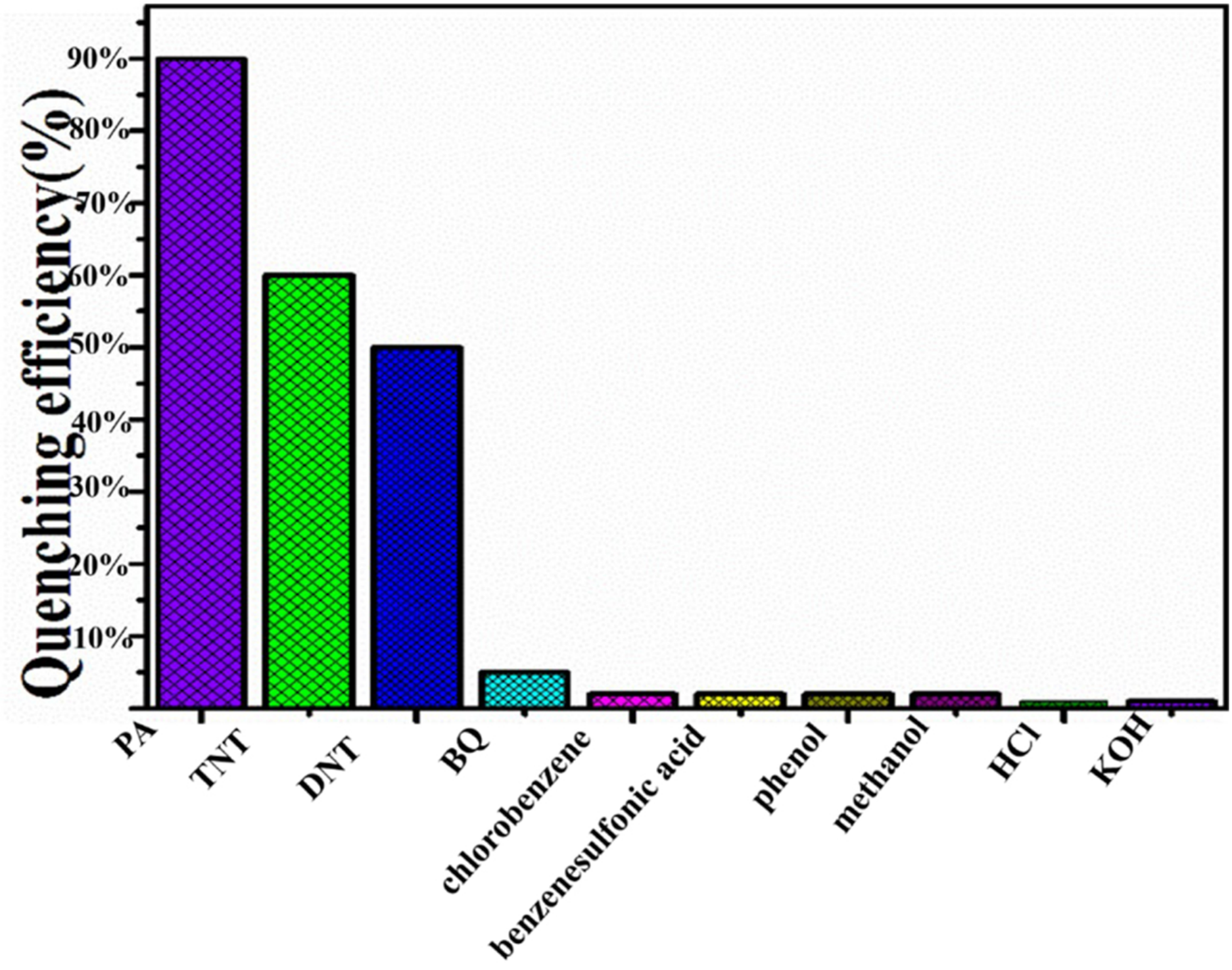
Quenching efficiency(%)
90%
80%
70%
60%
50%
40%
30%
20%
10%
PA
TNT
DNT
BQ
chlorobenzene
benzenesulfonic acid
phenol
methanol
HCl
KOH

Figure 14

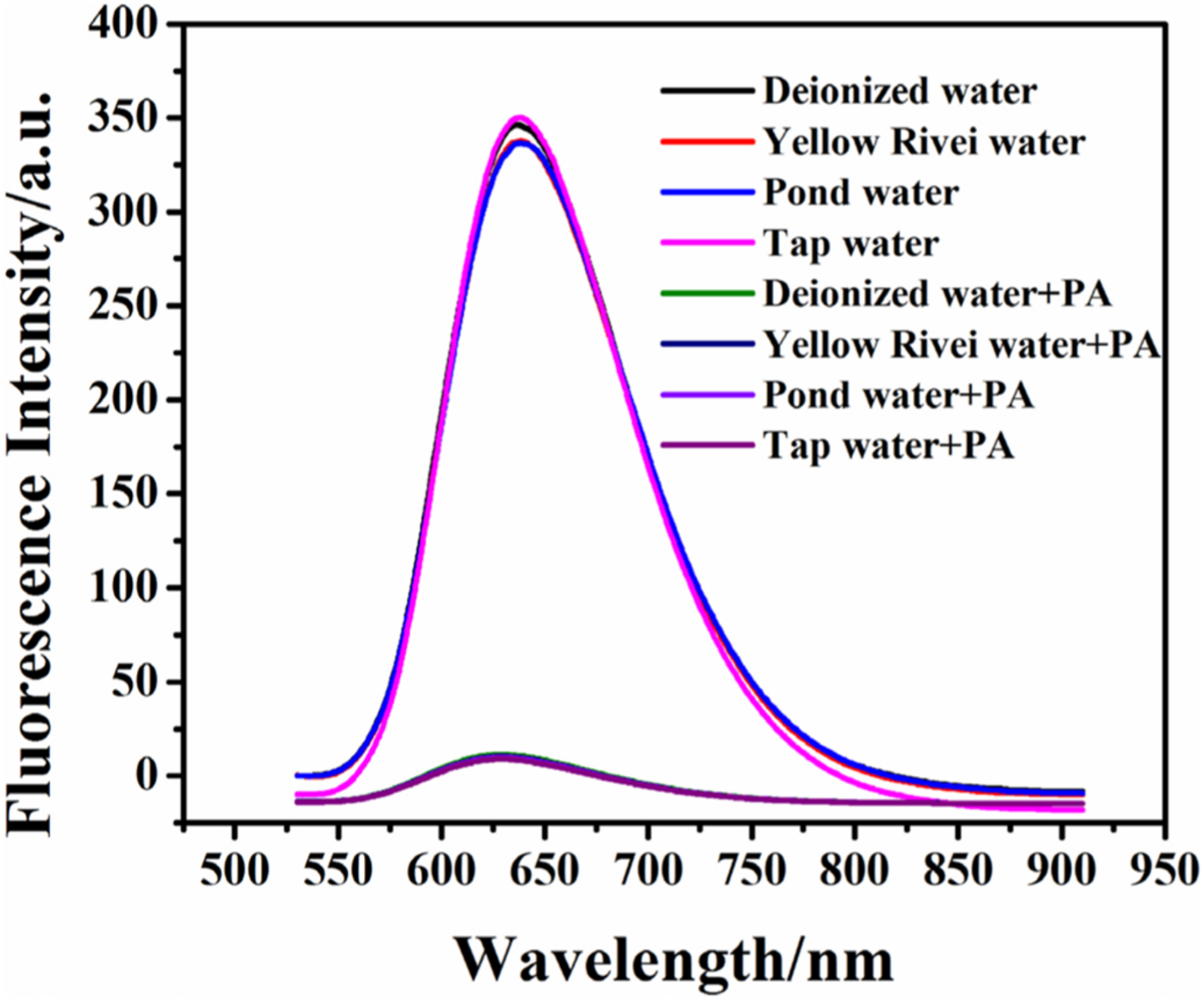
Fluorescence Intensity/a.u.
400
350
300
250
200
150
100
50
0
500
550
600
650
700
750
800
850
900
950
Wavelength/nm
Deionized water
Yellow Rivei water
Pond water
Tap water
Deionized water+PA
Yellow Rivei water+PA
Pond water+PA
Tap water+PA

Figure 15

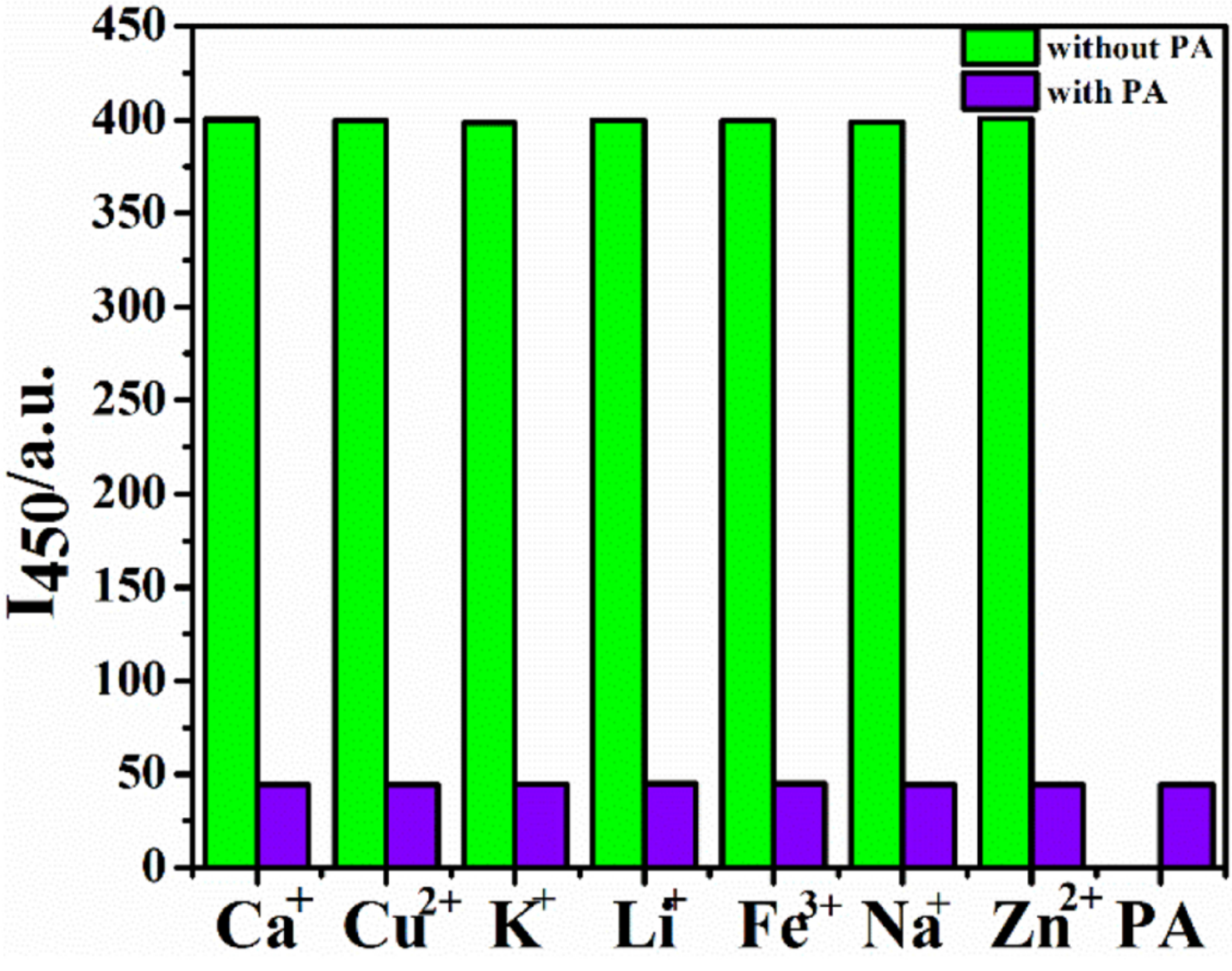
450
400
350
300
250
200
150
100
50
0
I450/a.u.
without PA
with PA
Ca+
Cu2+
K+
Li+
Fe3+
Na+
Zn2+
PA

Figure 16

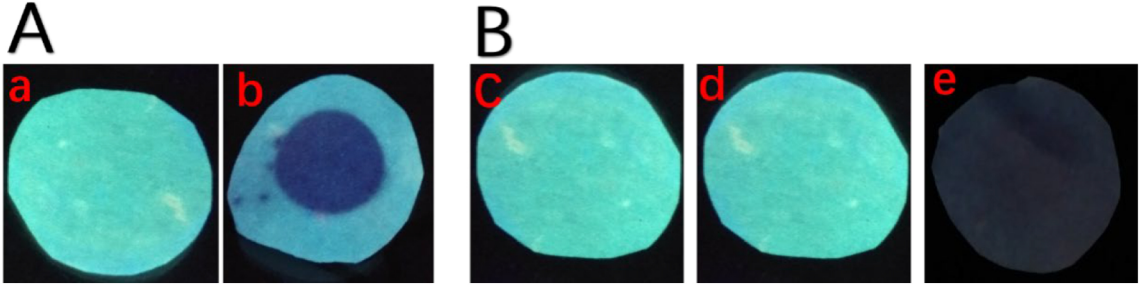

Figure 17

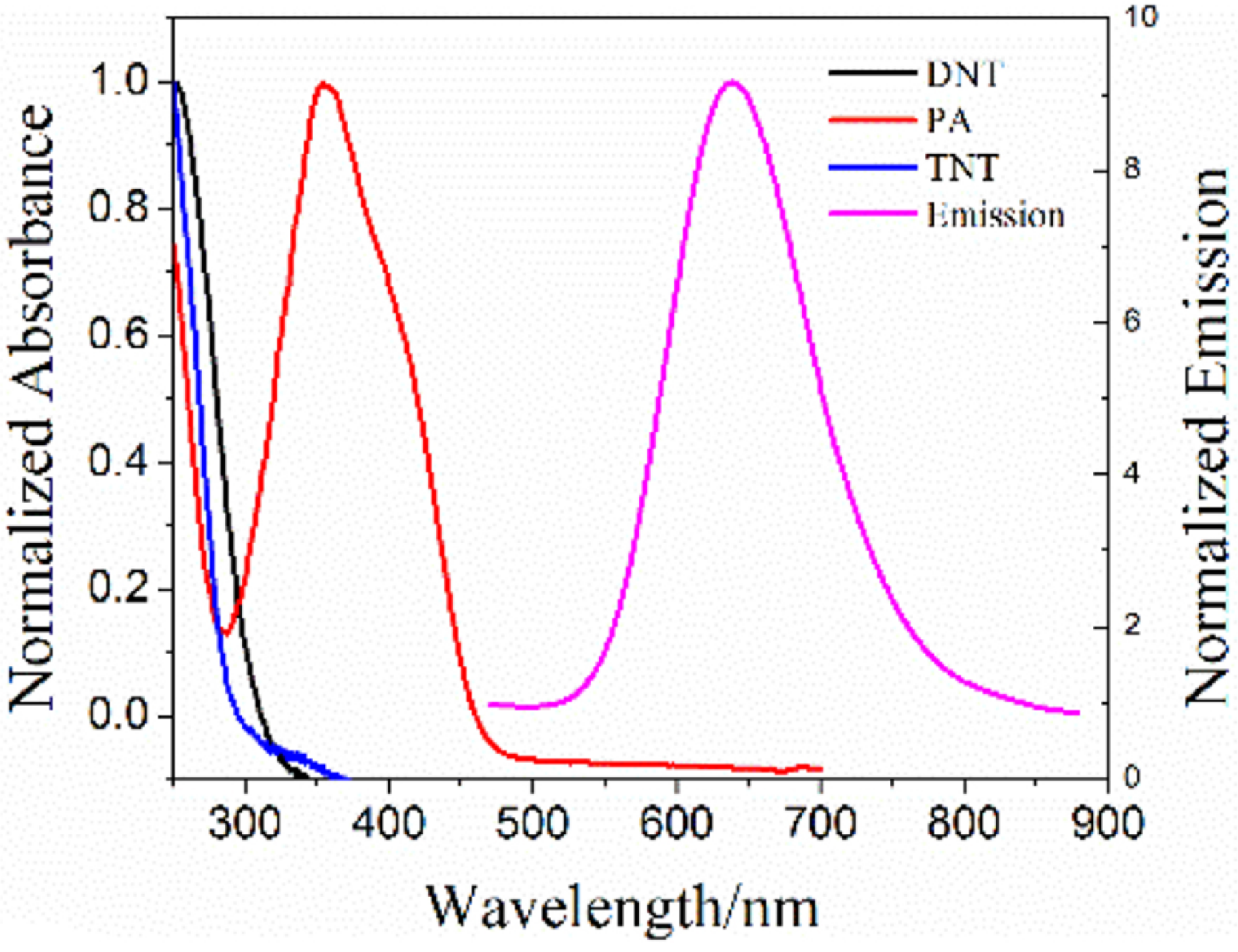
Normalized Absorbance
1.0
0.8
0.6
0.4
0.2
0.0
300
400
500
600
700
800
900
Wavelength/nm
DNT
PA
TNT
Emission
10
8
6
4
2
0
Normalized Emission

Figure 18

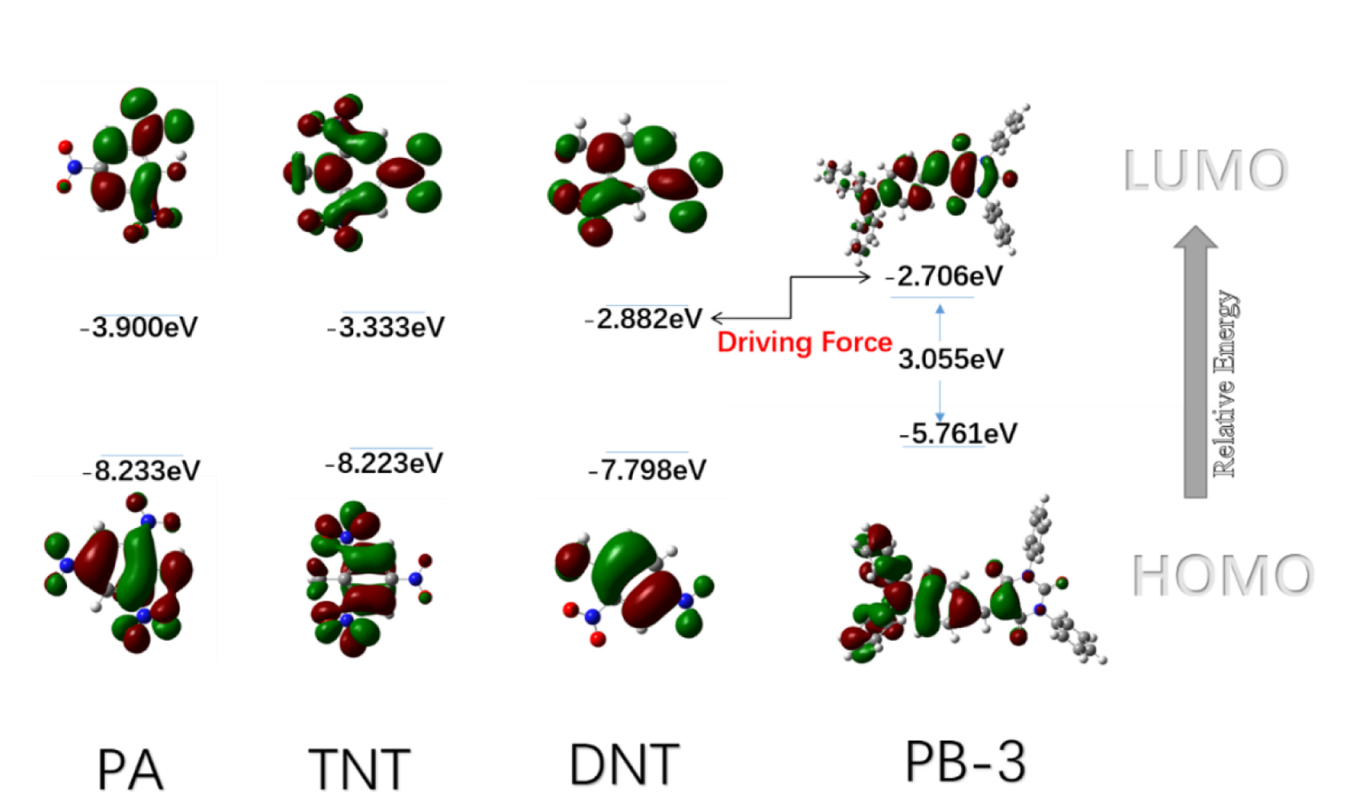
LUMO
-2.706eV
-3.900eV
-3.333eV
-2.882eV
Driving Force
3.055eV
-5.761eV
Relative Energy
-8.233eV
-8.223eV
-7.798eV
HOMO
PA
TNT
DNT
PB-3

Figure 19